The Astrophysical Journal, 888:96 (20pp), 2020 January 10 https://doi.org/10.3847/1538-4357/ab60a5

Predictions of Cosmic Microwave Background Foreground Dust Polarization Using Velocity Gradients

Yue Hu[1,2], Ka Ho Yuen[2], and A. Lazarian[2]
[1] Department of Physics, University of Wisconsin-Madison, Madison WI, USA; alazarian@facstaff.wisc.edu
[2] Department of Astronomy, University of Wisconsin-Madison, Madison WI, USA
Received 2019 October 12; revised 2019 November 18; accepted 2019 December 4; published 2020 January 14

Abstract

Observations of fluctuations in the cosmic microwave background provide information about primordial inhomogeneities in the universe. However, the B-mode polarization of the inflationary gravitational wave is contaminated by the Galactic foreground polarized radiation arising from dust aligned by interstellar magnetic fields. To trace magnetic fields, we use the Velocity Gradient Technique (VGT), which employs modern understanding of the nature of magnetohydrodynamic turbulent motions. In this paper, we combine the VGT with Principal Component Analysis (PCA) to improve the accuracy of magnetic field tracing. We apply the VGT–PCA to the high-resolution neutral hydrogen data from the GALFA-H I survey to predict the polarization of dust. We report that the predicted directions of dust polarization provide good correspondence with those reported by *Planck* 353 GHz, with the alignment measure between the two $\simeq 0.79 \pm 0.01$. We show that our results statistically agree with the *Planck* polarization in terms of magnetic field tracing. We find that the variation of dust emission efficiency across the sky is small. Using our maps of predicted polarization, we calculate the ratio of the E- and B-modes, and show that $\mathrm{BB/EE} \simeq 0.53 \pm 0.10$, which is similar to the result from *Planck* polarization.

Unified Astronomy Thesaurus concepts: Interstellar magnetic fields (845); Interstellar medium (847); Cosmic microwave background radiation (322)

1. Introduction

The fluctuations in the cosmic microwave background (CMB) polarization, which can be decomposed into "electric" (E) and "magnetic" (B) components, contain important information on the evolution of the early universe (Lewis 2003; Planck Collaboration et al. 2016d, 2016e; Manzotti et al. 2017). In particular, the measurement of CMB B-modes offers the possibility of studying the cosmological origin of inflationary gravitational waves (BICEP2 Collaboration et al. 2014; Ferreira et al. 2014; Kamionkowski & Kovetz 2016; Planck Collaboration et al. 2016d). However, the polarized thermal emission from diffuse Galactic dust is the main foreground present in measurements of the CMB polarization at frequencies above 100 GHz (Planck Collaboration et al. 2014a, 2015a, 2018c). The CMB B-mode signal is therefore contaminated by the Galactic dust foreground polarization arising from complicated interstellar magnetic fields (Jones 1989; Kovetz & Kamionkowski 2015; Voshchinnikov et al. 2016). To get insight into the CMB B-mode signal, a comprehensive picture of Galactic polarized foreground is essential to disentangle the spectral energy distribution of dust and CMB polarization across frequencies. The recent *Planck* survey gives full-sky polarization maps of dust emission (Planck Collaboration et al. 2018c). However, the polarization fraction is theoretically determined by the dust column along the line of sight (LOS) and the angle of the mean magnetic field in the plane of the sky (Planck Collaboration et al. 2014a). At high Galactic latitude regions, dust emissivity is low (Planck Collaboration et al. 2014b) and the polarization fraction is minimal (Planck Collaboration et al. 2016a). It is, therefore, challenging to characterize the complete Galactic foreground polarization using polarized dust emission. Nevertheless, even this minimal galactic polarization can present a challenge in measuring the weak B-mode signal.

The approach of studying magnetic fields with the Velocity Gradient Technique (VGT) has been a fast-developing branch of interstellar medium magnetic field studies. For instance, Velocity Centroid Gradients (VCGs; González-Casanova & Lazarian 2017; Yuen & Lazarian 2017a, 2017b) were first proposed to trace the magnetic field using the fact that in magnetohydrodynamic (MHD) turbulence, eddies are elongated along the magnetic field direction surrounding the eddies (Goldreich & Sridhar 1995; Lazarian & Vishniac 1999). Aside from velocity centroids, using the velocity information contained in the thin velocity channel map was also explored by Lazarian & Pogosyan (2000) and Yuen et al. (2019). The velocity gradients in such narrow velocity channels are shown to be more accurate in tracing magnetic fields. With that development, the VGT has already been successfully applied to a wide range of column densities, from diffuse transparent gas (Yuen & Lazarian 2017a; Hu et al. 2018; González-Casanova & Lazarian 2019; Hu et al. 2019b) to molecular self-absorbing dense gas (Hu et al. 2019a, 2019c), as well as to the estimation of magnetization level (Lazarian et al. 2018a; Hu et al. 2019c). Although the practical application of VGT is affected by the quality of data (Yuen et al. 2018), Hu et al. (2018) explored the noise suppression method for VGT and showed that Principal Component Analysis (PCA) could increase the accuracy of VGT in tracing magnetic fields.

PCA is originally a technique used in image processing and image compression. Regarding astrophysical applications, PCA was applied to obtain the turbulence spectrum from observations (Brunt & Heyer 2002a, 2002b), as well as to study turbulence anisotropies (Heyer et al. 2008). Because the principal components of gradients decomposed by PCA are more anisotropic, we use the gradients of the decomposed principal components as an alternative tool to trace the interstellar magnetic fields and predict the Galactic foreground polarization, denoted as the VGT–PCA technique.

In what follows, we illustrate the theoretical foundation of tracing the magnetic field based on MHD turbulence anisotropy

in Section 2. In Section 3, we describe the full algorithm in implementing the VGT–PCA. In Section 4, we apply VGT–PCA to a vast range of GALFA-H I data and make comparisons with *Planck* polarization. In Section 5, we discuss the modeling of the three-dimensional Galactic magnetic field, and the possible application and further development of VGT–PCA. In Section 6, we give our conclusions.

2. Theoretical Consideration

2.1. Theory of MHD Turbulence

Goldreich & Sridhar (1995) established the theoretical foundation of magnetic field tracing techniques through MHD turbulence statistics. Considering the Kolmogorov cascade with the injection velocity $v_l \simeq l_\perp^{\frac{1}{3}}$, Goldreich & Sridhar (1995) predicted that incompressible MHD turbulence is anisotropic, i.e., turbulent eddies are elongated along the direction of the magnetic field. The derivation in Goldreich & Sridhar (1995) is provided in the frame of the mean field, which was also the accepted frame for all theoretical constructions prior to that study.

However, the theory of turbulent reconnection in Lazarian & Vishniac (1999) showed that the GS95 relations are valid not in the mean field reference frame, but in the reference frame of individual eddies. In Lazarian & Vishniac (1999), the theory of turbulent reconnection explained that magnetic tension force resists all other types of magnetic field motion, except the rotating motion of eddies together with magnetic field lines in the direction perpendicular to magnetic fields local to the eddy. For the VGT, the concept of a local magnetic field frame is crucial. This concept was supported by numerical simulations and is well established by now (Cho & Vishniac 2000; Cho & Lazarian 2002, 2003).

It is because the turbulent motions are aligned with the local direction of the magnetic field that one can obtain the detailed structure of the magnetic field by studying velocity gradients, not just its mean direction. Understanding $\perp$ and $\parallel$ in this local direction sense, one can use the GS95 relation between the parallel and perpendicular eddy sizes, i.e., $l_\parallel \simeq l_\perp^{\frac{2}{3}}$, to see that the motions within the smallest eddies are the most aligned with the local magnetic fields.

Considering that the eddies due to turbulent reconnection freely mix with the magnetic field perpendicular to their direction, one can easily understand that the velocity fluctuations are expected to follow the the Kolmogorov scaling $V_{l,\perp} \sim l_\perp^{1/3}$, and therefore, the gradients are going to be the largest at the smallest scale $v_{l,\perp}/l_\perp \simeq l_\perp^{-2/3}$. It is also obvious that the measured velocity gradients are perpendicular to the magnetic field at the smallest resolved scales, i.e., they trace well the magnetic field in the turbulent volume. Note that similar to the case of far-infrared polarimetry, one should turn the direction of gradients by 90° to obtain the magnetic field direction.

The statistics of the velocity fluctuation are not directly available from observations. To get insight into velocity statistics, Lazarian & Pogosyan (2000, 2004) and Kandel et al. (2017) developed the theory of statistics of the Position–Position–Velocity (PPV) spectroscopic data cubes. They showed that intensity fluctuations in PPV cubes can arise due to turbulent velocities along the LOS. This effect of velocity crowding causes velocity caustics. It was shown that when the velocity channel width Δv and velocity dispersion δv satisfy the criterion

$$\Delta v^2 < \delta v^2, \tag{1}$$

this velocity channel is considered a thin velocity channel. Velocity fluctuation can dominate in this thin channel, due to the effect of velocity caustics. Based on this theory, Lazarian et al. (2018a) and Hu et al. (2019b) proposed using fluctuations of velocity within thin velocity channel maps to reveal the information on velocity gradients.

2.2. Polarized Thermal Dust Emission

Measuring the fraction of polarized thermal dust emission deepens our understanding of the diffuse ISM and also helps the search for inflationary gravitational wave B-mode polarization in the CMB. The Stokes parameters I, Q, U describe the polarization state of thermal dust emission. For constant magnetic field orientation and polarization fraction along the LOS, the integral equations of the Stokes parameters for linear dust polarization are defined as

$$\begin{aligned} Q &= \int p_{\max} R \cos(2\psi)\cos^2\gamma dI \\ U &= \int p_{\max} R \sin(2\psi)\cos^2\gamma dI \\ p &= \frac{\sqrt{Q^2+U^2}}{I} = p_{\max} RF \cos^2\gamma, \end{aligned} \tag{2}$$

where γ is the angle between the magnetic field and the plane of the sky (POS), ψ is the polarization angle, $p_{\max}$ is the maximum value of the polarization fraction, R is the Rayleigh reduction factor (i.e., the efficiency of grain alignment), and F is the depolarization factor (Planck Collaboration et al. 2015a). The theory of grain alignment predicts (see Lazarian & Hoang 2007) that radiative torques (RATs) are capable of aligning well the grains with the magnetic field in diffuse interstellar medium, provided that the grains precess fast in the ambient magnetic field. This is the case for silicate grains, but not for the non-silicate ones (see Lazarian & Hoang 2019).

Once the Stokes parameters $Q(\hat{n})$ and $U(\hat{n})$ have been measured as functions of spherical polar coordinates θ, ϕ (where $\hat{n}$ denotes a unit vector pointing at the polar angle $\theta \in [0, \pi]$ and azimuth $\phi \in [0, 2\pi]$) on the full-sky polarization, we have the polarization tensor:

$$P(\hat{n}) = \frac{1}{\sqrt{2}}\begin{bmatrix} Q(\hat{n}) & U(\hat{n})\sin\theta \\ U(\hat{n})\sin\theta & -Q(\hat{n})\sin^2\theta \end{bmatrix}. \tag{3}$$

The polarization tensor field on the sphere can be expanded in terms of basis functions that are gradients and curls of spherical harmonics $Y_{lm}(\hat{n})$:

$$P(\hat{n}) = \sum_{l=2}^{\infty}\sum_{m=-l}^{l}[a_{lm}^E Y_{lm}^E(\hat{n}) + a_{lm}^B Y_{lm}^B(\hat{n})]. \tag{4}$$

The expansion coefficients are given by

$$\begin{aligned} a_{lm}^E &= \int P(\hat{n}) Y_{lm}^{E*}(\hat{n}) d\hat{n} \\ a_{lm}^B &= \int P(\hat{n}) Y_{lm}^{B*}(\hat{n}) d\hat{n}. \end{aligned} \tag{5}$$

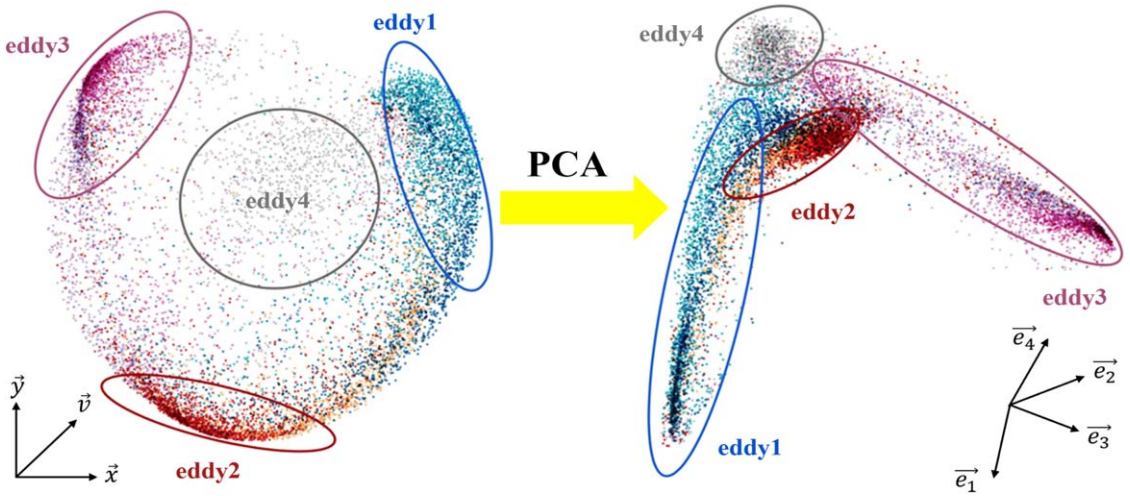

Figure 1. An illustration of how PCA works on PPV cubes. Supposing there exist four crucial velocity components, i.e., eddy1/2/3/4, in the original PPV cube (i.e., in the $\boldsymbol{x}$–$\boldsymbol{y}$–$\boldsymbol{v}$ space; see the left panel), the implementation of PCA converts these components to a set of linearly independent variables called principal components (see the right panel). The principal components are located at a new orthogonal basis formed by their corresponding eigenvectors (i.e., the $\boldsymbol{e}_1 - \boldsymbol{e}_2 - \boldsymbol{e}_3 - \boldsymbol{e}_4$ space), which are oriented along the direction of the large axis of each principal component. The length of the large axis is positively proportional to its corresponding eigenvalue, whose physical meaning is closely related to the value of the turbulence velocity dispersion δv^2. In particular, those larger eddies correspond to the largest-scale contributions of turbulence eddies along the LOS $\delta v^2 \simeq l^{\frac{2}{3}}$, where l is the scale of the eddy. The significance of eddy1/2/3/4 in the new space is therefore enhanced through PCA.

The angular cross-power spectra are now

$$\langle a_{lm}^{X*} a_{l'm'}^{X'} \rangle = C_l^{XX'} \delta_{ll'} \delta_{mm'}, \tag{6}$$

where $X = \{E; B\}$, $\langle ... \rangle$ denotes the ensemble average, and δ is the delta function. In general, both the foreground dust polarization and CMB polarization contribute to the spectra. However, it is difficult to separate the contribution from the CMB E- and B-mode as the expected signals from inflation and late-time reionization are expected to be small. In this case, accurate assessment and modeling of the Galactic foreground are crucial to the subtraction of the foreground dust polarization to $C_l^{\rm EE}$ and $C_l^{\rm BB}$.

3. Methodology

3.1. Principal Gradient Component Analysis

PCA is widely used in image processing and image compression, which effectively decomposes an image of size N^2 into $n < N$ eigenmaps. PCA uses an orthogonal linear transformation to convert a set of possibly correlated variables to a set of linearly independent variables called principal components (Hotelling 1933). Intuitively, PCA can be thought of as fitting an n-dimensional ellipsoid to the data, where each orthogonal axis of the ellipsoid represents a principal component. This fitting in PPV cube is implemented through the calculation of the covariance matrix, which gives the covariance between each velocity channel. The eigenvalues of the covariance matrix correspond to the length of the large axis of each principal component, and the eigenvectors are oriented along the direction of the large axis. If some eigenvalue is small, then the variance along that axis and the contribution from its corresponding principal component are also small. We can therefore (i) remove the noise by omitting small eigenvalues and their corresponding principal components from our representation of the data set (Hu et al. 2018), and (ii) enhance the contribution from crucial components by projecting the original data set into the new orthogonal basis formed by the eigenvectors.

As illustrated in Figure 1, we suppose that there exist four kinds of balls with different colors blue, red, purple, and gray mixing in a pool. In PCA's picture, each ball represents each data point in the original PPV cube, and the four colors correspond to four crucial velocity components, eddy1/2/3/4. The question is how to classify those balls based on their colors (or how to separate those eddies through PCA). To solve it in our daily life, the simplest way is to prepare four boxes first and label them by color (blue, red, purple, or gray). We randomly pick up a ball and distinguish its color, which is equivalent to calculating the covariance matrix. We then drop each individual ball into the corresponding box based on its color (i.e., the dropping step is equivalent to the projection of the original data set onto the new orthogonal basis). After this classification, we find that we need much larger boxes (i.e., the size of the box represents the corresponding eigenvalue) to store blue or purple balls than red or gray balls. We can then say that the number of blue and purple balls are much larger than the number of red and gray balls in the pool, i.e., the contribution from eddy1 and eddy3 is, therefore, more significant than the one from eddy2 and eddy4, and there is little change in the pool even if we remove the red and gray balls. More importantly, in these new classified boxes, we can play with single-color balls without any effect from the others.

In the world of PCA, we project those eddies onto a new orthogonal eigenspace, i.e., the $\boldsymbol{e}_1 - \boldsymbol{e}_2 - \boldsymbol{e}_3 - \boldsymbol{e}_4$ space, by weighting the original PPV cube with the eigenvectors calculated through PCA. In the new space, the length of the eddy's large axis is positively proportional to its corresponding eigenvalue, whose physical meaning is closely related to the value of the turbulence velocity dispersion δv^2. In particular, those larger eddies correspond to the largest-scale contributions of the turbulence eddies along the LOS $\delta v^2 \simeq l^{\frac{2}{3}}$, where l is the scale of the eddy. The significance of eddy1 and eddy3 in the new space is therefore separated and signified through PCA. Hu et al. (2018) used the PCA as a tool to provide the preliminary processing of the spectroscopic data, and they found that the structure in the new eigenspace becomes more anisotropic. As velocity gradients scale

as $v_{l,\perp}/l_\perp \simeq l_\perp^{-2/3}$ (see Section 2), the highly anisotropic components significantly contribute to the accuracy of velocity gradients in tracing magnetic fields. We, therefore, see the possibility of improving VGT by combining it with PCA, which can then extract the most crucial velocity components.

In this work, we follow the assumption used in Hu et al. (2018)—treat the PPV cube $\rho(x, y, v)$ as the probability density function of three random variables x, y, v. Then, we defined the modified covariance matrix (Brunt & Heyer 2002a, 2002b) and the eigenvalue equation for this covariance matrix as

$$S(v_i, v_j) \propto \int dxdy\rho(x, y, v_i)\rho(x, y, v_j) - \int dxdy\rho(x, y, v_i) \int dxdy\rho(x, y, v_j), \quad (7)$$

$$\boldsymbol{S} \cdot \boldsymbol{u} = \lambda \boldsymbol{u}, \quad (8)$$

where $\boldsymbol{S}$ is the covariance matrix with matrix element $S(v_i, v_j)$, with $i, j = 1, 2, \ldots, n_v$. λ are the eigenvalues associated with the eigenvector matrix $\boldsymbol{u}$. Note that $\boldsymbol{u}$ consists of eigenvectors $\boldsymbol{u}_i$ sorted in a rank based on the decreasing order of λ_i, with elements u_{ij}, $i, j = 1, 2, \ldots, n_v$. Thereafter, we project the PPV cube onto the direction of each eigenvector $\boldsymbol{u}_i$, by weighting the channel $\rho(x, y, v_j)$ with the corresponding eigenvector u_{ij}. Hence, we get the corresponding eigenmap $I_i(x, y)$:

$$I_i(x, y) = \sum_j^{n_v} u_{ij} \cdot \rho(x, y, v_j). \quad (9)$$

By repeating the procedure for each eigenvector $\boldsymbol{u}_i$, we finally get a set of eigenmaps $I_i(x, y)$, with $i = 1, 2, \ldots, n_v$. From an individual eigenmap $I_i(x, y)$, the gradient orientation at each individual pixel (x_m, y_n) is calculated by convolving the image with 3×3 Sobel kernels:

$$G_x = \begin{pmatrix} -1 & 0 & +1 \\ -2 & 0 & +2 \\ -1 & 0 & +1 \end{pmatrix}, G_y = \begin{pmatrix} -1 & -2 & -1 \\ 0 & 0 & 0 \\ +1 & +2 & +1 \end{pmatrix}$$

$$\nabla_x I_i(x, y) = G_x * I_i(x, y)$$
$$\nabla_y I_i(x, y) = G_y * I_i(x, y)$$
$$\psi_{gi} = \tan^{-1}\left(\frac{\nabla_y I_i}{\nabla_x I_i}\right), \quad (10)$$

where $\nabla_x I_i(x, y)$ and $\nabla_y I_i(x, y)$ are the x and y components of the gradients, respectively. ψ_{gi} is the pixelized gradient map for each $I_i(x, y)$. The subblocking method, proposed by Yuen & Lazarian (2017a), is applied after the pixelized gradient map is established. Within a subblock of interests, the distributions of the gradient vector orientation appear as a more accurate Gaussian profile with the increment the size of the subregion. In this case, the mean gradient direction becomes more well defined, and the alignment between the gradient and magnetic field becomes more accurate. By taking the Gaussian fitting peak value of the gradient distribution in a selected subblock, we obtain the mean direction of the magnetic field in that subregion. The subblock averaging method therefore can increase the significance of important statistical measures and suppress noise in a subregion of the gradient field.

In observations, the magnetic field orientation is inferred from the polarization angle ψ, which can be derived from the Stokes Q, U maps using the relation

$$\psi = \frac{1}{2}\tan^{-1}\left(\frac{U}{Q}\right). \quad (11)$$

However, the orientation of the magnetic field measured by gradients is different from that of dust polarization: gradients measure the sectional magnetic field along the LOS, while polarization measures the density-weighted accumulated magnetic field directions along the LOS. As a result, we suggest comparing the Stokes-parameter-equivalent Q_g and U_g of the gradient-induced magnetic field to those of polarization:

$$Q_g(x, y) = \sum_{i=1}^{n} I_i(x, y)\cos(2\psi_{gi}(x, y))$$
$$U_g(x, y) = \sum_{i=1}^{n} I_i(x, y)\sin(2\psi_{gi}(x, y))$$
$$\psi_g = \frac{1}{2}\tan^{-1}\left(\frac{U_g}{Q_g}\right), \quad (12)$$

where $I_i(x, y)$ is the ith eigenmap, and $\psi_{gi}(x, y)$ is the gradient angle calculated from $I_i(x, y)$ with the subblock averaging implemented. The mock polarization angle ψ_g is then defined correspondingly, which gives a probe of the POS magnetic field orientation after rotating 90°. Note that in constructing $Q_g(x, y)$ and $U_g(x, y)$, one can project the data onto the subset of the dominant principal components but not onto all of them, i.e., $n < n_v$, especially when the smallest eigenvalues of the covariance matrix are dominated by noise. In this work, we do not distinguish the noise subset and use $n = n_v$.

3.2. Alignment Measure

We make comparisons with the *Planck* 353 GHz polarized dust signal data from the *Planck* 3rd Public Data Release (DR3) 2018 of High Frequency Instrument (Planck Collaboration et al. 2018a),[3] where the signal-to-noise ratio (S/N) of the dust emission is maximum at low Galactic latitude regions. The *Planck* observations provide Stokes parameter maps I, Q, and U, so the POS magnetic field orientation angle θ can be derived from the Stokes parameters: $\theta = \psi - \pi/2$.

The relative orientation between the POS magnetic field predicted by VGT–PCA and the one inferred from *Planck* polarization is quantified by the alignment measure (AM):

$$\mathrm{AM} = 2\left(\langle\cos^2\theta_r\rangle - \frac{1}{2}\right), \quad (13)$$

where θ_r is the angular difference between the magnetic field vectors predicted from VGT–PCA and the vector inferred from polarization in a single subblock. Because AM is insensitive to the sign of the gradient, e.g., $\mathrm{AM}(\theta) = \mathrm{AM}(-\theta)$, it is advantageous to test the performance of each method. We expect to get $\mathrm{AM} = 1$ in most cases, which implies a perfect alignment, i.e., the rotated ψ_g is parallel to the POS magnetic field. The AM has been widely

[3] Based on observations obtained with *Planck* (http://www.esa.int/Planck), an ESA science mission with instruments and contributions directly funded by ESA Member States, NASA, and Canada.

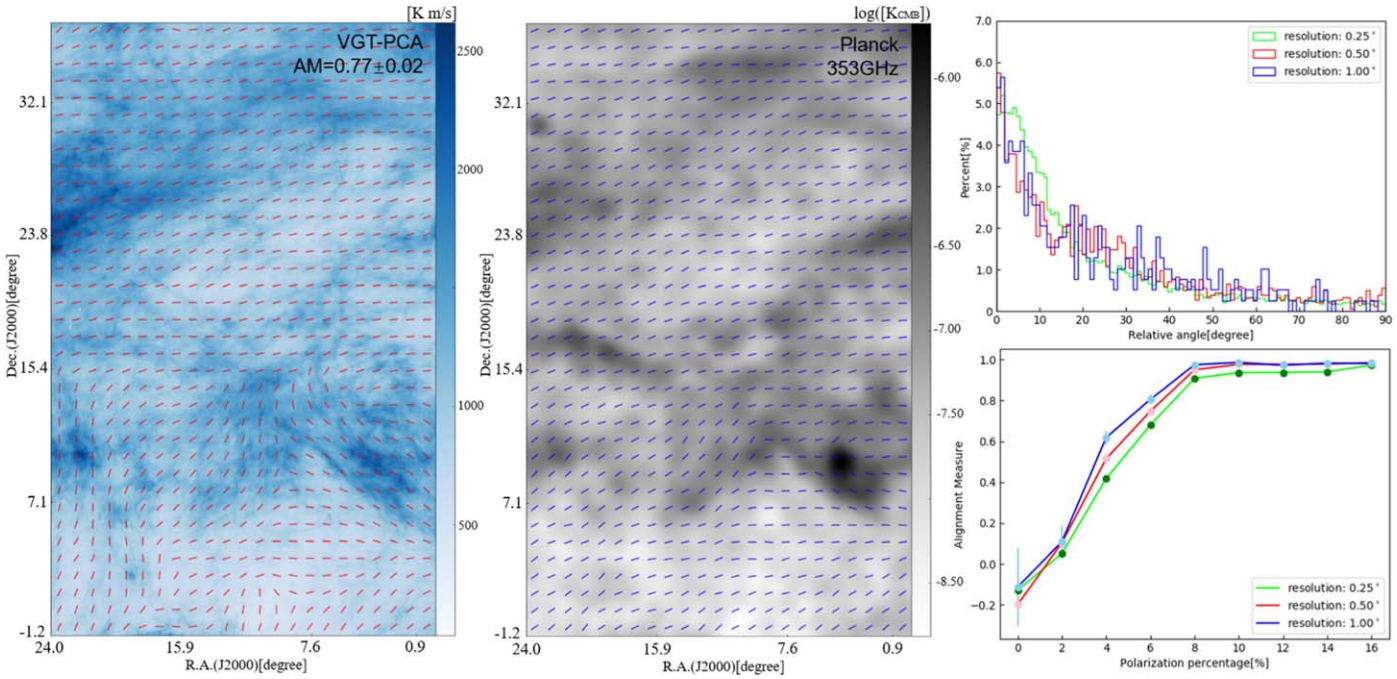

Figure 2. The morphology of the POS magnetic fields on the sky patch with R.A. from 0.°0 to 24.°0 and decl. from −1.°2 to 37.°1. Left: the magnetic field predicted from VGT–PCA (red segments) with resolution ≃1°. Middle: the magnetic fields inferred from *Planck* polarization (blue segments). The background color map of VGT–PCA is the GALFA-H I data integrated intensity from −32 to 23 km s^{-1}. Right top: the histogram of the relative orientation between the magnetic field predicted by VGT–PCA and the one inferred from *Planck* polarization. Right bottom: the variation of the AM with respect to the polarization percentage.

used in gradients studies (González-Casanova & Lazarian 2017, 2019; Yuen & Lazarian 2017a, 2017b; Hu et al. 2018, 2019a, 2019b, 2019c). Obviously, it is equivalent to $\langle \cos 2\theta_r \rangle$, which was used recently in Clark & Hensley (2019).

4. Results

4.1. Magnetic Field Morphology in Low Galactic Latitude Regions

In this work, we use the high spatial and spectral resolution H I data from Data Release 2 (DR2) of the Galactic Arecibo *L*-Band Feed Array H I survey (GALFA-H I) with the Arecibo 305 m radio antenna (Peek et al. 2018). GALFA-H I has a gridded angular resolution of $1' \times 1'$ per pixel, a spectral resolution of 0.18 km s^{-1}, and a brightness temperature noise of ≃40 mK rms per 1 km s^{-1} integrated channel over 13,000 deg^2 of sky. The full GALFA-H I data is separated into three sets: East (denoted by A, close to the east of the Galactic Plane), North (denoted by B, close to the Galactic north pole), and West (denoted by C, close to the west of Galactic Plane). Each data set is divided into five individual subregions (see Appendix A for details about each region).

For illustration, we take the region A1, which stretches from R.A. ≃ 0.°0 to 24° and decl. ≃−1.°5 to 37.°0, as an example. This region spans from galactic latitude $b \simeq -30°$ below the Galactic Plane to $b \simeq -60°$ i.e., close to the Galactic south pole. We analyze the H I data within velocity range −23 to 32 km s^{-1}, which contains the main structure of the H I data.

Following the recipe of VGT–PCA, we show the morphology of POS magnetic fields inferred from VGT–PCA with resolution ≃1° in Figure 2. We make a comparison with the magnetic field morphology inferred from *Planck* polarization and get AM = 0.77 ± 0.02, which indicates the overall good alignment between VGT–PCA and *Planck*. The *Q*, *U* maps from *Planck* are smoothed with FWHM = 1°. The uncertainty is given by the standard error of the mean, i.e., the standard deviation divided by the square root of the sample size.

As an analogy to the VGT, the minimum tracing resolution, i.e., the subblock size, depends on the histogram of the gradients' orientation. The histogram should be a well-defined Gaussian distribution so that the most probable angle can be found out by Gaussian fitting. Once the minimum scale is determined, one can trace the magnetic field in any scale larger than the minimum threshold. In view of this, we test three resolutions (0.°25, 0.°50, and 1.°0) for VGT–PCA and plot the histogram of the relative orientation between the magnetic field predicted by VGT–PCA and the one inferred from *Planck* polarization in Figure 2. We see that for all of the three resolutions, the histogram shows a convex Gaussian profile with a peak value around zero.

In view of this, a difference between the magnetic field predicted by VGT–PCA and the one inferred from *Planck* polarization exists. We consider two possible reasons. One contribution is from the fitting uncertainty of the subblock averaging method. It has been reported that the velocity gradient orientations in a subblock would form a Gaussian distribution in which the peak of the Gaussian fit reflects the statistically most probable magnetic field orientation in this subblock (Yuen & Lazarian 2017a). As the area of the sampled region increases, the precision of the magnetic field traced through the use of a Gaussian block fit becomes more and more accurate. However, there exists an uncertainty in fitting the Gaussian distribution, and the most probable value of the Gaussian distribution has its own standard deviation σ. Those factors would contribute to the overall uncertainty of the gradients' calculation (Hu et al. 2019b), which is expected to be the systematic error in our calculation. The second factor is possibly the uncertainty in the polarization measurements.

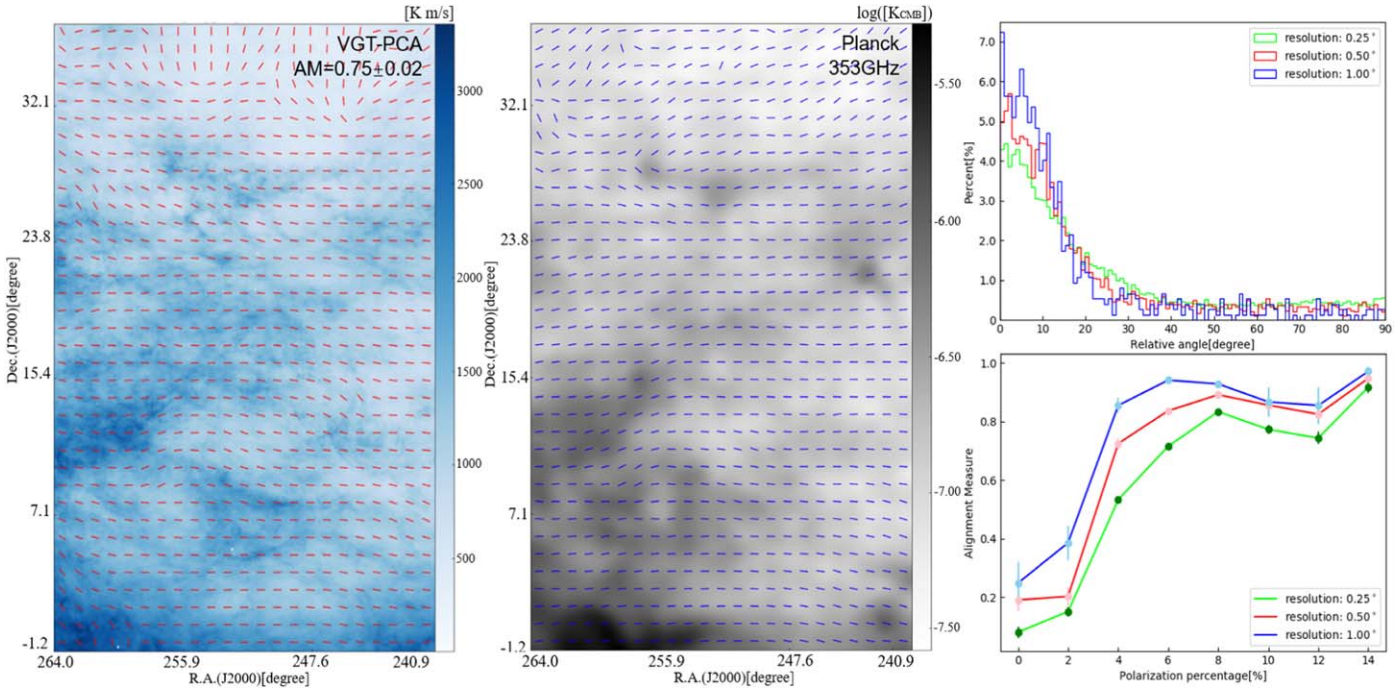

Figure 3. The morphology of the POS magnetic fields on the sky patch with R.A. from 240.°0 to 264.°0 and decl. from −1.°2 to 37.°1. Left: the magnetic field predicted from VGT–PCA (red segments) with resolution ≃1°. Middle: the magnetic fields inferred from *Planck* polarization (blue segments). The background color map of VGT–PCA is the GALFA-H I data intensity integrated from −32 to 23 km s^{-1}. Right top: the histogram of the relative orientation between the magnetic field predicted by VGT–PCA and the one inferred from *Planck* polarization. Right bottom: the variation of the AM with respect to the polarization percentage.

The uncertainty in dust polarimetry becomes significant in the case where the grains are not aligned. Grain alignment theory suggests that grain alignment is driven mainly by RATs, but the grains can become misaligned in a number of circumstances (Lazarian 2003). For instance, in the absence of sufficiently intense radiation, the orientation of dust grains is random (Lazarian & Hoang 2007). In view of this, we plot the correlation between the AM and polarization percentage p in Figure 2. We take the average value of AM in each bin of the polarization percentage. We see that AM is positively proportional to the polarization percentage and gets saturated when $p \geqslant 8\%$. Therefore, the insufficient polarization flux in polarimetry measurements contributes to the deviation between the magnetic field predicted by VGT–PCA and the one inferred from *Planck* polarization.

Except for the subregion A1 ,which is close to the Galactic south pole, we repeat our analysis for the subregion C1, which spans from galactic latitude $b \simeq 30°$ above the Galactic plane to $b \simeq 45°$. The POS magnetic field morphology is shown in Figure 3. The AM $= 0.75 \pm 0.02$ indicates the overall good alignment between VGT–PCA and *Planck* in C1. We see similar results in terms of the histogram of the relative orientation and the variation of the AM concerning the polarization percentage. Moreover, we apply those analyses to all low-latitude regions, i.e., data set A and C; we see that all of them show the good alignment between VGT–PCA and *Planck* and the positive correlation between the alignment and polarization percentage (see Appendix A for details about each region). Therefore, we conclude that VGT–PCA shows statistically good performance in terms of characterizing the Galactic dust polarization comparing with the *Planck* polarization. We see the possibility of correcting the issue of insufficient polarization percentage through VGT–PCA. The resultant morphology of POS magnetic fields inferred from *Planck* polarization and VGT–PCA is shown in Figure 4.

4.2. Magnetic Field Morphology in High Galactic Latitude Regions

Based on the advanced understanding of MHD turbulence in the ISM, VGT–PCA shows good ability in tracing the magnetic field morphology at low Galactic regions (see Section 4.1) compared with the *Planck* polarization. As for high Galactic regions, H I gas still follows the property of MHD turbulence. Therefore, we expect that VGT–PCA also works in high Galactic regions. Figure 5 takes the subregion B3, which includes the Galactic north pole, as an example. We do see there is an agreement between VGT–PCA and *Planck* in relatively high-intensity regions. From the histogram, we find that the peak value of the relative orientation between VGT–PCA and *Planck* is located at ≃20° ± 0.°79, with standard deviation ≃22.°5 for all three resolutions. While the histogram is more dispersed, the alignment is still increasing with the increase of the polarization percentage.

The resultant morphology of POS magnetic fields inferred from *Planck* polarization and VGT–PCA is shown in Figure 6. VGT–PCA in high Galactic latitude regions gives a moderate overall alignment, i.e., AM $= 0.45 \pm 0.01$. The rapidly varying magnetic fields and low S/N at high Galactic latitude regions are two possible reasons for the misalignment between VGT–PCA and *Planck*. The polarization percentage p is theoretically determined by the dust column density along the LOS and the angle of the mean magnetic field concerning the plane of the sky (Planck Collaboration et al. 2014a). However, at high Galactic latitude regions, the dust emissivity is low (Planck Collaboration et al. 2014b), and the magnetic fields are varying rapidly (Planck Collaboration et al. 2015b, 2016a).

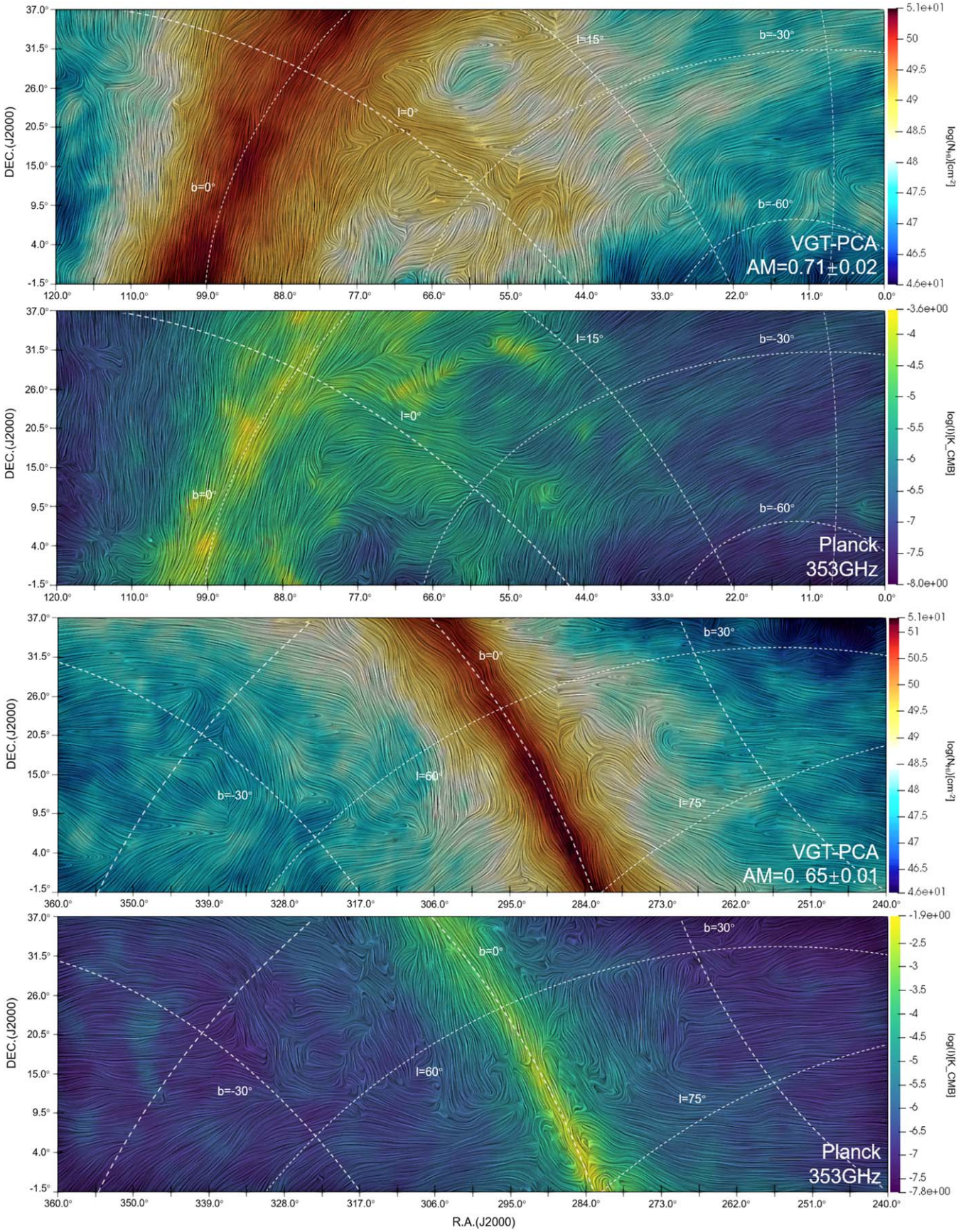

Figure 4. The morphology of the POS magnetic fields at low Galactic latitude regions inferred from *Planck* polarization (the second and the fourth columns) and VGT–PCA (the first and the third columns). The background color maps of VGT–PCA is the H I column density map integrated from -90 to 90 km s^{-1}. The magnetic field is visualized using the Line Integral Convolution (LIC).

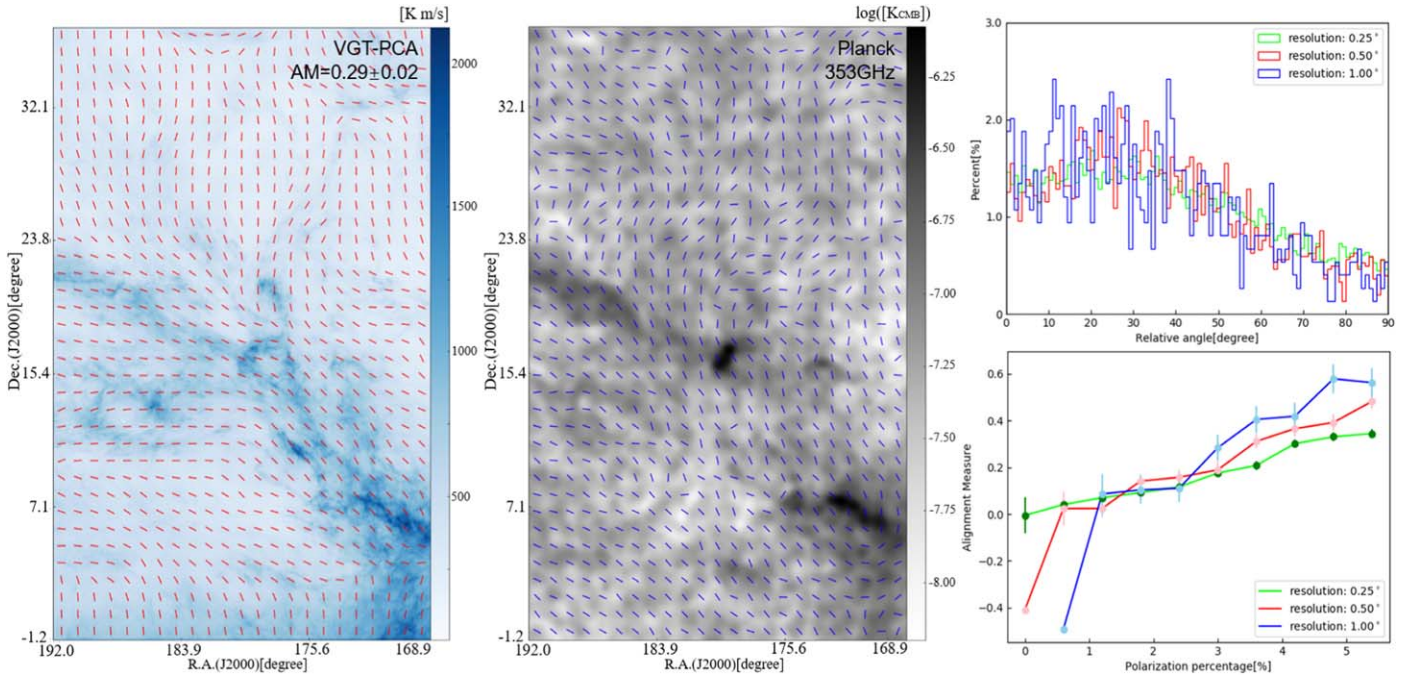

Figure 5. The morphology of the POS magnetic fields on the sky patch with R.A. from 168.°0 to 192.°0 and decl. from −1.°2 to 37.°1. Left: the magnetic field predicted from VGT–PCA (red segments) with resolution ≃1°. Middle: the magnetic fields inferred from *Planck* polarization (blue segments). The background color map of VGT–PCA is the GALFA-H I data integrated from −41 to 14 km s^{-1}. Right top: the histogram of the relative orientation between the magnetic field predicted by VGT–PCA and the one inferred from *Planck* polarization. Right bottom: the variation of the AM with respect to the polarization percentage.

Therefore, the polarization fraction is minimal near the Galactic north pole. Besides, the noise level in polarization data is estimated to be higher at high Galactic latitude regions (Clark et al. 2015). Those factors obscure the accurate measurement of the Galactic dust polarization and the magnetic field at high Galactic latitude regions. The third possibility is that the disagreement might come from the selection of the velocity range in H I data. The H I data contain information on the structures in the selected velocity ranges, while polarization is accumulating the information along the LOS. Also, we expect the boundary effect will also cause the disagreement to appear near the image's boundary.

Also, we use the magnetic field inferred from starlight polarization catalogs (Berdyugin et al. 2014) as a relative comparison in high Galactic latitude regions ($b > 30°$). In Figure 7, we plot the histogram of the relative angle between the polarization from 566 stars and VGT–PCA in corresponding positions. We see that the histogram statistically satisfies a Gaussian distribution, with standard deviation $\sigma = 14.°4$ and expectation value $\mu \simeq 5°$. We can, therefore, conclude that VGT–PCA statistically shows agreement with the starlight polarization.

4.3. Polarization Percentage

The polarization percentage p can be derived from Stokes parameters U and Q using the definition in Equation (2) and the intensity map from *Planck* polarization. As for the polarization percentage p_g from pseudo-Stokes parameters U_g and Q_g, we use a similar definition to p and use the integrated H I intensity map. In Figure 8, we show the correlation between the polarization percentage derived from *Planck* polarization (denoted as p) and VGT–PCA (denoted as p_g), corresponding to the same coordinate. We bin the measured polarization percentage in uniformly spaced bins with an interval of 0.01. We see that p_g shows a linear correlation with p at low Galactic latitude regions. However, the value of p_g is about four times larger than p. We expect that the ratio of 4 is the systematic difference between H I and polarized dust emission data caused by the grain alignment efficiency.

Generally, it is difficult to model grain alignment efficiency across the sky with different physical conditions. Planck Collaboration et al. (2018b) reported a maximum polarization fraction $p_{\max} \simeq 22\%$ using 353 GHz polarization data. As a result, the dust grain alignment efficiency should be intrinsically similar to $p_{\max}$. In Figure 9, we see a linear correlation between the polarization percentage predicted by VGT–PCA and *Planck* polarization, which indicates that the variation of grain alignment efficiency is small across the sky. Figure 9 gives the sky maps of polarization percentage obtained from VGT–PCA using GALFA-H I data and *Planck* 353 GHz dust polarization. We see that VGT–PCA shows similar structures to *Planck* polarization in terms of polarization percentage. Note that this prediction of polarization percentage is incomplete without the knowledge of the inclination angle γ.

4.4. Decomposition of E-/B-modes

The full-sky CMB polarization field can be decomposed into E and B components that are signatures of distinct physical processes. To decompose the E-mode and B-mode, we modified the template used in Clark et al. (2015):

$$Q^*(x, y) = p^* \cdot I_{353}(x, y) \cdot \cos(2\psi^*(x, y))$$
$$U^*(x, y) = p^* \cdot I_{353}(x, y) \cdot \sin(2\psi^*(x, y)), \quad (14)$$

where p^* is the polarization percentage derived from either VGT–PCA or *Planck* polarization, I_{353} is the intensity of *Planck* 353 GHz polarized dust emission, and ψ^* is the polarization angle defined from either VGT–PCA or *Planck* polarization. In

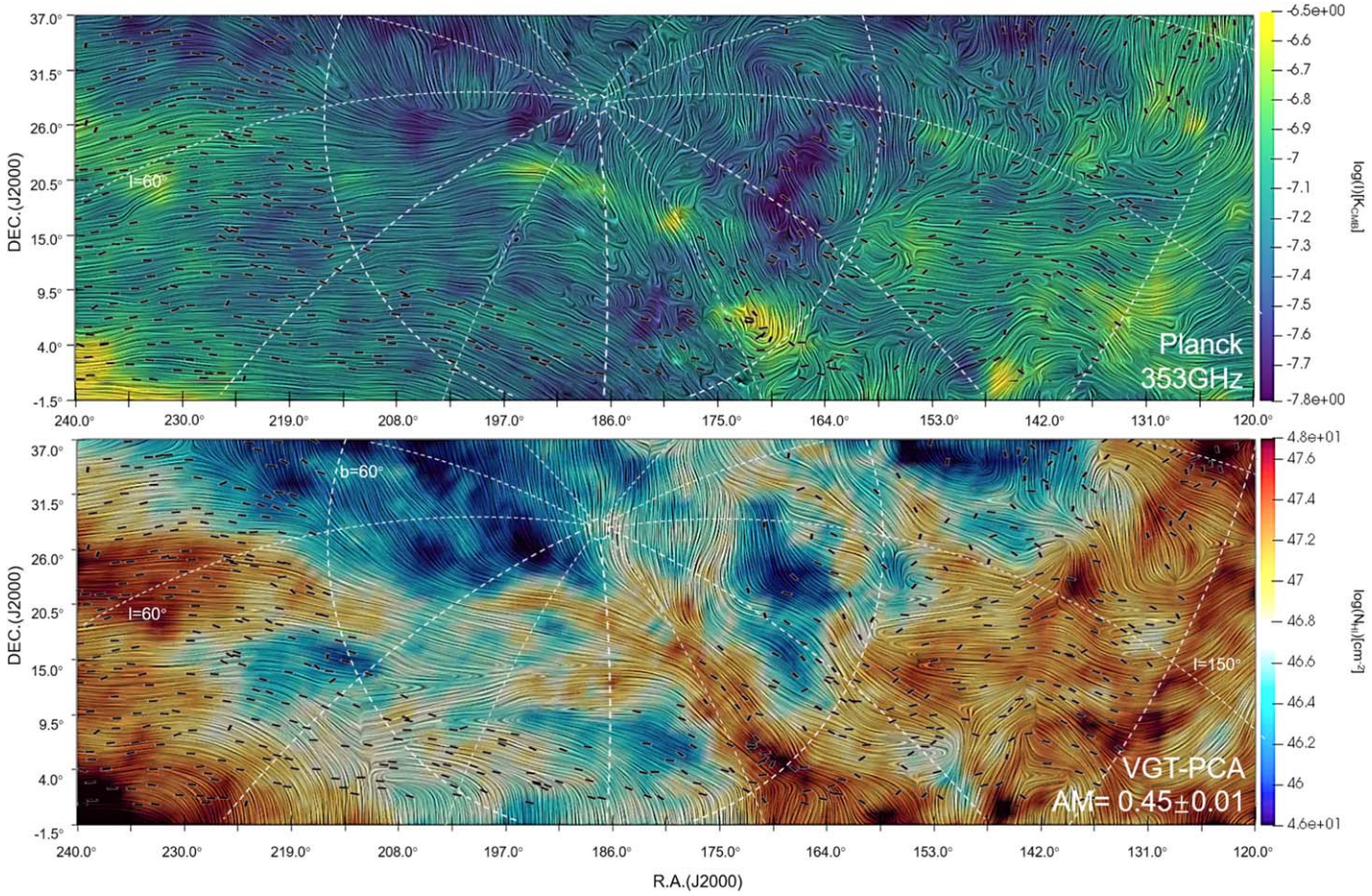

Figure 6. The morphology of the POS magnetic fields at high Galactic latitude regions inferred from *Planck* polarization (top) and VGT–PCA (bottom). The background color maps of VGT–PCA is the H I column density map integrated from -90 to 90 km s^{-1}. The magnetic field is visualized using Line Integral Convolution (LIC). Black pseudo-vectors represent starlight polarization angles obtained from the Berdyugin et al. (2014) catalogs.

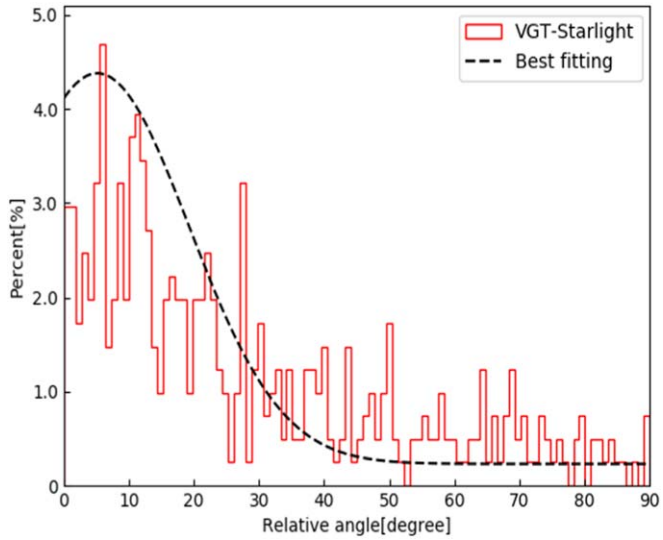

Figure 7. The histogram of relative angle between the magnetic fields in Figure 6 derived from VGT–PCA and starlight polarization obtained from the Berdyugin et al. (2014) catalogs. The standard deviation σ is 14°.14.

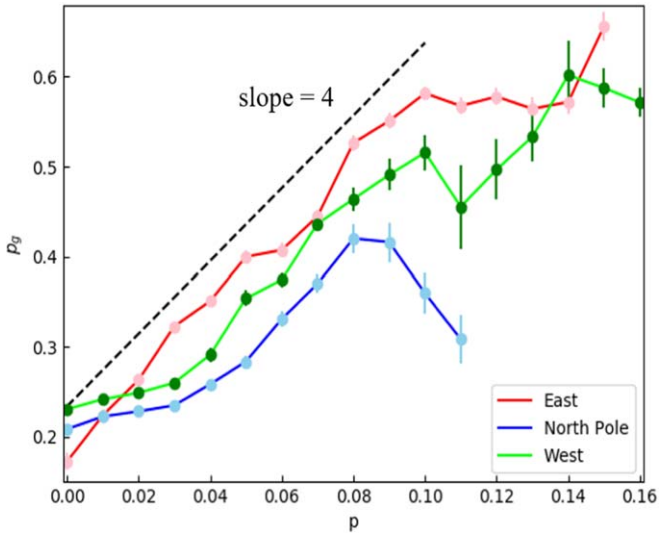

Figure 8. The correlation between the polarization percentage derived from *Planck* polarization (x-axis, denoted by p) and VGT–PCA (y-axis, denoted by p_g).

Clark et al. (2015), the polarization percentage is assumed to be ideally unity. However, this assumption is only reasonable over a small patch of sky. For a large patch of sky, it is indispensable to take the polarization percentage into account.

The derived Stokes maps Q^* and U^* at 1° resolution are converted to HEALPix2 format (Górski et al. 2005) with HEALPix resolution of $N_{\rm side} = 512$, following Planck Collaboration et al. (2016d). The Stokes Q^* and U^* maps are

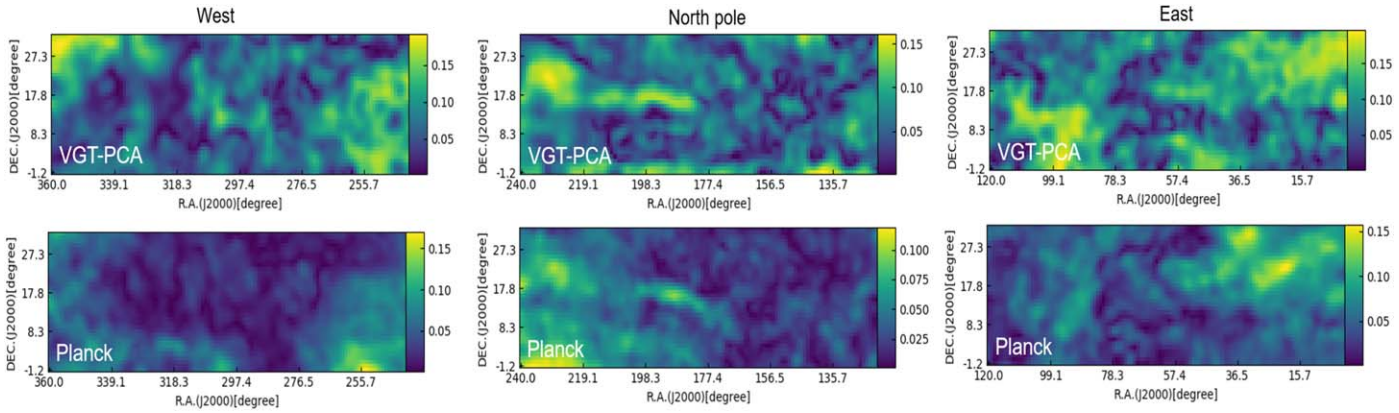

Figure 9. Sky maps of the polarization fraction obtained from VGT–PCA (top) using GALFA-H I data and *Planck* 353 GHz dust polarization (bottom) with effective resolution $\simeq 1°$.

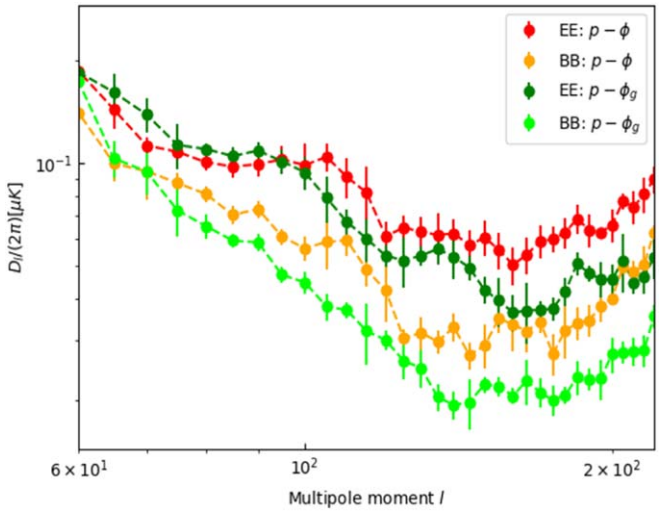

Figure 10. The cross-power spectra for the template maps constructed from VGT–PCA and *Planck* polarization. The y-axis is $D_l = l(l+1)C_l$. The symbol p and ϕ indicate that we are using *Planck* data for the template, while p_g indicates the polarization percentage and polarization angle obtained from VGT–PCA. The spectra are plotted using the full GALFA data set.

then decomposed into $C_l^{\rm EE}$ and $C_l^{\rm BB}$ using the "anafast" routine of HEALPix.

Figure 10 shows the cross-power spectra for the template maps constructed from VGT–PCA and *Planck* polarization, using the whole set of GALFA-H I data. The multipole moment ranges from $l = 60$ to $l = 250$, which is limited by the resolution of the input maps. We find that the spectra constructed from VGT–PCA (i.e., the combination of p and ϕ_g) show a smaller magnitude than the one from *Planck* polarization (i.e., the combination of p and ϕ). We expect that one possible reason is the contribution from the CMB polarization in *Planck* HFI data. The discrepancy between the magnetic fields traced by two different methods might also cause the deviation. Also, we see that the EE cross-power spectra derived from *Planck* polarization show a larger amplitude than the BB spectra for both combinations. We find the mean ratio between EE and BB cross-power spectrum derived from VGT–PCA to be 0.53 ± 0.10, while it is 0.61 ± 0.11 for *Planck* polarization. The results coincide with those of Planck Collaboration et al. (2016c), which show a systematic difference between the amplitudes of the Galactic dust B- and E-modes, BB/EE $\simeq 0.5$.

5. Discussion

5.1. Three-dimensional Galactic Magnetic Fields Modeling

The detection of primordial B-mode polarization in the CMB is a top topic in cosmology. Although several missions are scheduled to search for the B-mode (BICEP2 Collaboration et al. 2014; Ferreira et al. 2014; Kamionkowski & Kovetz 2016; Planck Collaboration et al. 2016d; Remazeilles et al. 2018; Hanany et al. 2019; Lee et al. 2019), the contamination from polarized dust emission of the foreground is still an obstacle. To remove the foreground, the model of three-dimensional Galactic magnetic fields, which constrains the LOS structures of the magnetized and dusty ISM, is therefore crucial. However, generally, it is challenging to construct a comprehensive three-dimensional structure of the ISM and the magnetic field orientation along the LOS.

The advanced theories of MHD turbulence (Goldreich & Sridhar 1995; Lazarian & Vishniac 1999) and the statistics of the PPV data (Lazarian & Pogosyan 2000) provide one solution. Goldreich & Sridhar (1995) and Lazarian & Vishniac (1999) reveal that the anisotropic turbulence induces velocity fluctuations aligned with its local magnetic fields. Lazarian & Pogosyan (2000) gave the criterion on selecting thin velocity channels, in which the velocity fluctuations are dominating due to the effect of velocity caustics. Lazarian & Yuen (2018a) first combined these theories to trace the POS magnetic fields using the Velocity Channel Gradients (VChGs). González-Casanova & Lazarian (2019) extend this concept of thin velocity channels to study the 3D Galactic magnetic fields using H I data. González-Casanova & Lazarian (2019) initially constructed the 3D magnetic fields in PPV space by adding the velocity gradients in a way similar to the Stokes parameter (see Section 3). Later, Clark & Hensley (2019) also implemented this idea in establishing 3D magnetic fields in PPV space. Relying on the galactic rotation curve, González-Casanova & Lazarian (2019) successfully completed the 3D magnetic field modeling in the Milky Way, comparing it with stellar polarization. A similar idea is also expected to be available for VGT–PCA. The second way to establish the three-dimensional Galactic magnetic fields requires the knowledge of the inclination angle γ. For example, Equation (2) indicates that the predicted polarization percentage is overestimated without a picture of the three-dimensional magnetic field orientation.

5.2. Comparison with Earlier Works

Lu et al. (2019) demonstrated that VChGs could be used to produce synthetic maps of dust polarization from H I data. The VChGs were initially proposed by Lazarian & Yuen (2018a) to trace the magnetic field using thin velocity channels. It selects the data within the LOS velocity range $v_0 - \frac{\Delta v}{2} < v < v_0 + \frac{\Delta v}{2}$, where v_0 is the velocity corresponding to the central peak of the velocity profile along the LOS. The velocity channel width Δv and the velocity dispersion δv satisfy the criterion (Lazarian & Pogosyan 2000)

$$\Delta v^2 < \delta v^2. \tag{15}$$

However, in our work, we do not constrain the data within the range $v_0 - \frac{\Delta v}{2} < v < v_0 + \frac{\Delta v}{2}$, but integrate the pseudo-Stokes parameters obtained in each slice along the LOS. Lu et al. (2019) limit their work on a sky region, which stretches over R.A. from 215°.0 to 265°.0 and decl. from 6°.0 to 37°.5, to avoid the regions near the Galactic plane and the north Galactic pole. By making the synergy with PCA, we extend our prediction of dust polarization over the full GALFA-H I data set, which covers the Galactic plane, the north Galactic pole, and the south Galactic pole. Our work thus involves several different physical conditions. We further show that the grain alignment efficiency $\eta \simeq 25\%$, and its variation is small across the sky. It indicates that the Galactic magnetic fields cause the variation in polarized dust emission.

Clark & Hensley (2019) proposed predicting the dust polarization using H I in an alternatively way. Their work is based on the Rolling Hough Transform (RHT; see Clark et al. 2014), which requires linear structures in ISM. Compared with RHT, the VGT–PCA technique is parameter-free while RHT requires three parameters as inputs: a smoothing kernel diameter (DK), window diameter (DW), and intensity threshold (Z; Clark et al. 2014, 2015). Clark & Hensley (2019) predicted dust polarization across the full-sky region using HI4PI data. However, Clark & Hensley (2019) interpreted that the predominantly physical nature of the H I structures in thin velocity channel maps comes from Cold Neutral Media (CNM), without considering the velocity caustics effect (Lazarian & Pogosyan 2000). It thus calls into question (i) the physical nature of "H I fibers" and (ii) the distribution of CNM in the Galaxy. For the latter, Kalberla & Haud (2018) showed that the CNM is concentrated on the region near the Galactic plane, i.e., $|b| < 30°$, instead of the full sky.

5.3. Application to Giant Molecular Clouds

The approach of the gradients technique has been successfully tested to trace the local magnetic field from absorbing media for the case of ^{13}CO emission with different abundances and densities (González-Casanova et al. 2019), while Hsieh et al. (2019) numerically showed the availability of the gradient in tracing magnetic fields using synthetic molecular line maps of the CO isotopolog with different optical depths. Thereafter, in observation, Hu et al. (2019c) successfully applied the gradients technique to five low-mass star-forming regions using ^{13}CO as molecular tracer, while Hu et al. (2019a) expanded the technique into seven different molecular tracers in Giant Molecular Cloud Vela C. Importantly, we see that the magnetic field morphology obtained from VGT–PCA in the region corresponding to the molecular clouds Taurus and Perseus (see Appendix A, Figure 12) agrees with the results from *Planck* polarization and the VGT in Hu et al. (2019c). Therefore, we expect that VGT–PCA is also applicable to molecular clouds.

Due to the position of the solar system within the Galactic disk, the LOS inevitably crosses more than one molecular cloud. It is therefore impossible to use far-infrared polarimetry to study the local magnetic fields in most molecular clouds. Fortunately, VGT–PCA show advantages in dealing with multicloud issues. Theoretically, both VGT–PCA and dust polarization represent the direction of the projected magnetic field by accumulating information along the LOS. However, spectroscopic data often sample different regions of the molecular clouds compared to dust polarization. Spectroscopic data cubes can better identify the molecular cloud in velocity space with respect to polarization data. The background/foreground signals are therefore less important in the spectroscopic data cubes. VGT–PCA using molecular tracers would provide the information on the local magnetic field in the cloud, while polarization accumulates the information along the LOS. Combining the magnetic field traced from H I data, CO or other molecular tracer data, and polarized dust emission data, we see the possibility of figuring out the contribution from the Galactic foreground to polarized dust emission on molecular clouds.

5.4. Application within Synchrotron Polarization

VGT–PCA is one of the techniques that employ the properties of MHD turbulence to study magnetic fields. We expect that the application of VGT–PCA is not limited to molecular emission-line data. Lazarian et al. (2018b), Lazarian & Yuen (2018b), and Zhang et al. (2019) numerically show that the Synchrotron Intensity Gradients (SIGs) and Synchrotron Polarization Gradients (SPGs) can be used to trace the magnetic field component parallel to the LOS and even the three-dimensional magnetic field morphology. Because the foundation of SIGs and SPGs is still the anisotropy of MHD turbulence, we expect that VGT–PCA will be applicable to synchrotron data as well.

6. Conclusion

The inflationary gravitational wave B-mode polarization is contaminated by the Galactic foreground polarization arising from complicated interstellar magnetic fields. In this work, we explore a new way to trace the magnetic field and make predictions for the polarized dust emission using neutral hydrogen data. To summarize:

1. We develop VGT–PCA as a new tool in characterizing the Galactic dust polarization using only neutral hydrogen data, by creating a synergy of VGT and PCA. In particular:
   (a) We apply VGT–PCA to all high-resolution neutral hydrogen data from the GALFA-H I survey and make a comparison with the *Planck* polarized dust emission and stellar polarization data.
   (b) VGT–PCA shows statistically good agreement with the *Planck* polarization and stellar polarization in terms of magnetic field tracing.
   (c) We find that the alignment between VGT–PCA and the *Planck* polarization is positively proportional to the polarization percentage. We conclude that insufficient polarization flux is one factor that leads to the

misalignment of the VGT–PCA and *Planck* polarization.
2. We find that the polarization percentage predicted by VGT–PCA using the GALFA-H I data and *Planck* polarization is linearly correlated with a factor of 0.25, and its variation is small across the sky.
3. The full Galactic foreground templates can be constructed by using the Stokes parameter predicted by VGT–PCA. We show that the mean ratio between the EE and BB cross-power spectrum derived from VGT–PCA is 0.53 ± 0.10, which is in agreement with the results from the *Planck* measurement.
4. We claim that VGT–PCA as a modification of the VGT is advantageous in studying the magnetic field morphology and predicting the contribution from the Galactic foreground.

A.L. acknowledges the support of NSF grants AST 1715754 and 1816234. K.H.Y. acknowledges the support of NSF grant AST 1816234. Y.H. acknowledges the support of the NASA TCAN 144AAG1967. This publication utilizes data from the Galactic ALFA H I (GALFA H I) survey data set obtained with the Arecibo *L*-band Feed Array (ALFA) on the Arecibo 305 m telescope. The Arecibo Observatory is operated by SRI International under a cooperative agreement with the National Science Foundation (AST-1100968), and in alliance with Ana G. Méndez-Universidad Metropolitana and the Universities Space Research Association. The GALFA H I surveys have been funded by the NSF through grants to Columbia University, the University of Wisconsin, and the University of California. We acknowledge the use of NERSC TCAN computer time allocation.

Software: Julia (Bezanson et al. 2012), HEALPix (Górski et al. 2005), Paraview (Ahrens et al. 2005).

Appendix A
GALFA-H I Data Selection

In this work, the ensemble GALFA-H I data is separated into three data sets: East (A), North pole (B), and West (C). Each data set is divided into five individual subregions. The velocity range of each data set is selected, such that the majority of the Galactic neutral hydrogen gas is included. Table 1 gives the description of the GALFA-H I data set used in this work. The uncertainty on the AM is given by the standard error of the mean, i.e., the standard deviation divided by the square root of the sample size. Figures 11–16 show the morphology of the POS magnetic fields inferred from *Planck* polarization and VGT–PCA with resolution $\simeq 1^\circ$.

In Figure 11, we highlight the region of the Taurus molecular cloud. We see that the magnetic fields derived from VGT–PCA is well aligned with the magnetic fields inferred from *Planck* polarization. Earlier, Hu et al. (2019c) applied the VChGs technique (Lazarian & Yuen 2018a) to study the magnetic fields in the Taurus molecular cloud using ^{13}CO spectroscopic data. They showed that the magnetic fields inferred from ^{13}CO molecular data are also statistically similar to the magnetic fields inferred from *Planck* polarization. As both VGT–PCA and VChGs are tracing local magnetic fields using velocity gradients, it, therefore, encourages the study of the magnetic field properties in atomic and molecular gas, respectively.

In Figure 15, we find that there is a region in which the relative angle between VGT–PCA and *Planck* is approximately 45°, which is theoretically unexpected. One possible reason is the fitting uncertainty from the subblock averaging method. As explained in Section 4, there exists uncertainty in fitting the Gaussian distribution, and the most probable value of the Gaussian distribution has its standard deviation σ. Those factors would contribute to the overall uncertainty of the magnetic field calculation (Hu et al. 2019b). Subsequently, it was found that the σ of the distribution is correlated with the statistical mean magnetization of the subregion (Lazarian et al. 2018a). In this case, the deviation seen in Figure 15, upper-right corner, indicates that the properties or dynamics of H I gas in that region are different. For example, the supernova will change the dynamics of gas in its surroundings. In addition, we list the expectation value μ of the histogram of the relative alignment between the VGT–PCA and *Planck* 353 GHz dust polarization, with resolution $\simeq 1^\circ$ in Table 1. We see that μ gets

Table 1
Description of GALFA-H I Data Set Used in This Work

Data Set	Subregion	R.A.(J2000)	Decl.(J2000)	Velocity Range	AM	μ
East	A1	[0.°0, 24.°0]	[−1.°2, 37.°1]	[−32, 23 km s^{-1}]	0.77 ± 0.02	1.°21 ± 0.°72
	A2	[24.°0, 48.°0]	[−1.°2, 37.°1]	[−32, 23 km s^{-1}]	0.79 ± 0.01	2.°08 ± 0.°51
	A3	[48.°0, 72.°0]	[−1.°2, 37.°1]	[−32, 23 km s^{-1}]	0.67 ± 0.02	1.°8 ± 0.°67
	A4	[72.°0, 96.°0]	[−1.°2, 37.°1]	[−32, 41 km s^{-1}]	0.68 ± 0.01	6.°62 ± 0.°70
	A5	[96.°0, 120.°0]	[−1.°2, 37.°1]	[−23, 32 km s^{-1}]	0.64 ± 0.02	2.°14 ± 0.°79
North Pole	B1	[120.°0, 144.°0]	[−1.°2, 37.°1]	[−23, 32 km s^{-1}]	0.40 ± 0.02	0.°54 ± 0.°87
	B2	[144.°0, 168.°0]	[−1.°2, 37.°1]	[−41, 14 km s^{-1}]	0.35 ± 0.01	13.°82 ± 0.°83
	B3	[168.°0, 192.°0]	[−1.°2, 37.°1]	[−41, 14 km s^{-1}]	0.29 ± 0.02	20.°05 ± 0.°79
	B4	[192.°0, 216.°0]	[−1.°2, 37.°1]	[−32, 23 km s^{-1}]	0.51 ± 0.02	14.°91 ± 0.°77
	B5	[216.°0, 240.°0]	[−1.°2, 37.°1]	[−32, 23 km s^{-1}]	0.73 ± 0.02	4.°05 ± 0.°78
West	C1	[240.°0, 264.°0]	[−1.°2, 37.°1]	[−23, 32 km s^{-1}]	0.75 ± 0.02	1.°99 ± 0.°65
	C2	[264.°0, 288.°0]	[−1.°2, 37.°1]	[−23, 41 km s^{-1}]	0.45 ± 0.02	5.°66 ± 0.°88
	C3	[288.°0, 312.°0]	[−1.°2, 37.°1]	[−23, 32 km s^{-1}]	0.55 ± 0.02	7.°89 ± 0.°76
	C4	[312.°0, 336.°0]	[−1.°2, 37.°1]	[−32, 23 km s^{-1}]	0.61 ± 0.02	3.°56 ± 0.°68
	C5	[336.°0, 360.°0]	[−1.°2, 37.°1]	[−32, 23 km s^{-1}]	0.73 ± 0.01	3.°81 ± 0.°58

Note. The full GALFA-H I data set is separated into three parts. μ is the expectation value of the histogram of the relative alignment between the VGT–PCA and *Planck* 353 GHz dust polarization, with resolution $\sim 1^\circ$. The uncertainties on AM and μ are given by the standard error of the mean, i.e., the standard deviation divided by the square root of the sample size.

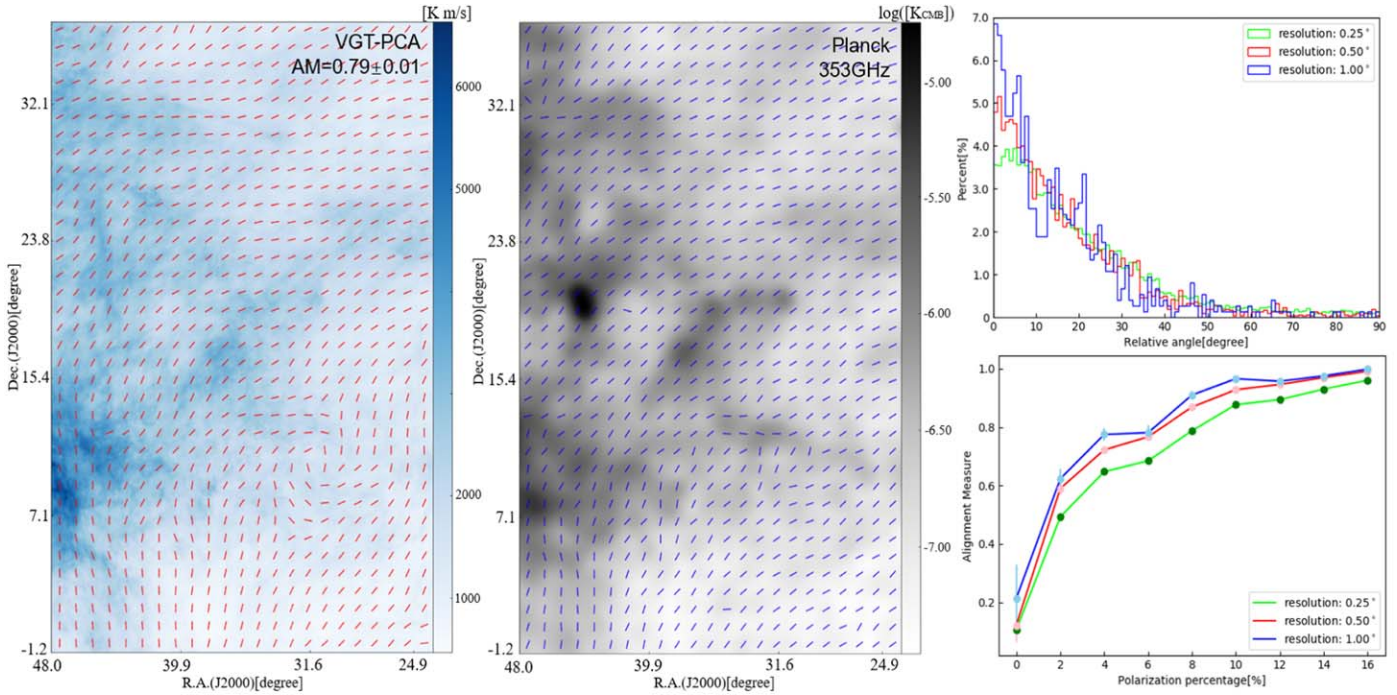

(a) A2

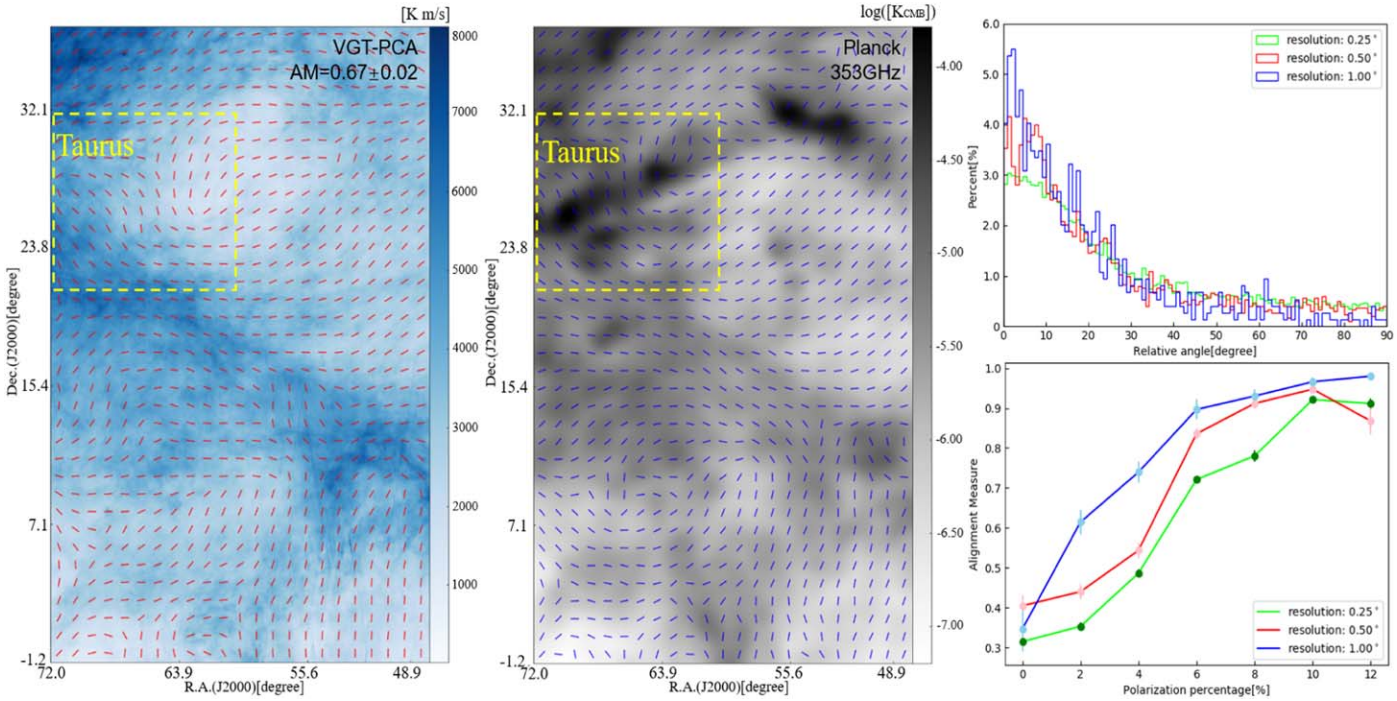

(b) A3

Figure 11. The morphology of the POS magnetic fields on the sky patch with (a): R.A. from 24.°0 to 48.°0 and decl. from −1.°2 to 37.°1, and (b): R.A. from 48.°0 to 72.°0 and decl. from −1.°2 to 37.°1. Left: the magnetic field predicted from VGT–PCA (red segments) with resolution ≃1°. Middle: the magnetic fields inferred from *Planck* polarization (blue segments). Right top: the histogram of the relative orientation between the magnetic field predicted by VGT–PCA and the one inferred from *Planck* polarization. Right bottom: the variation of the AM with respect to the polarization percentage.

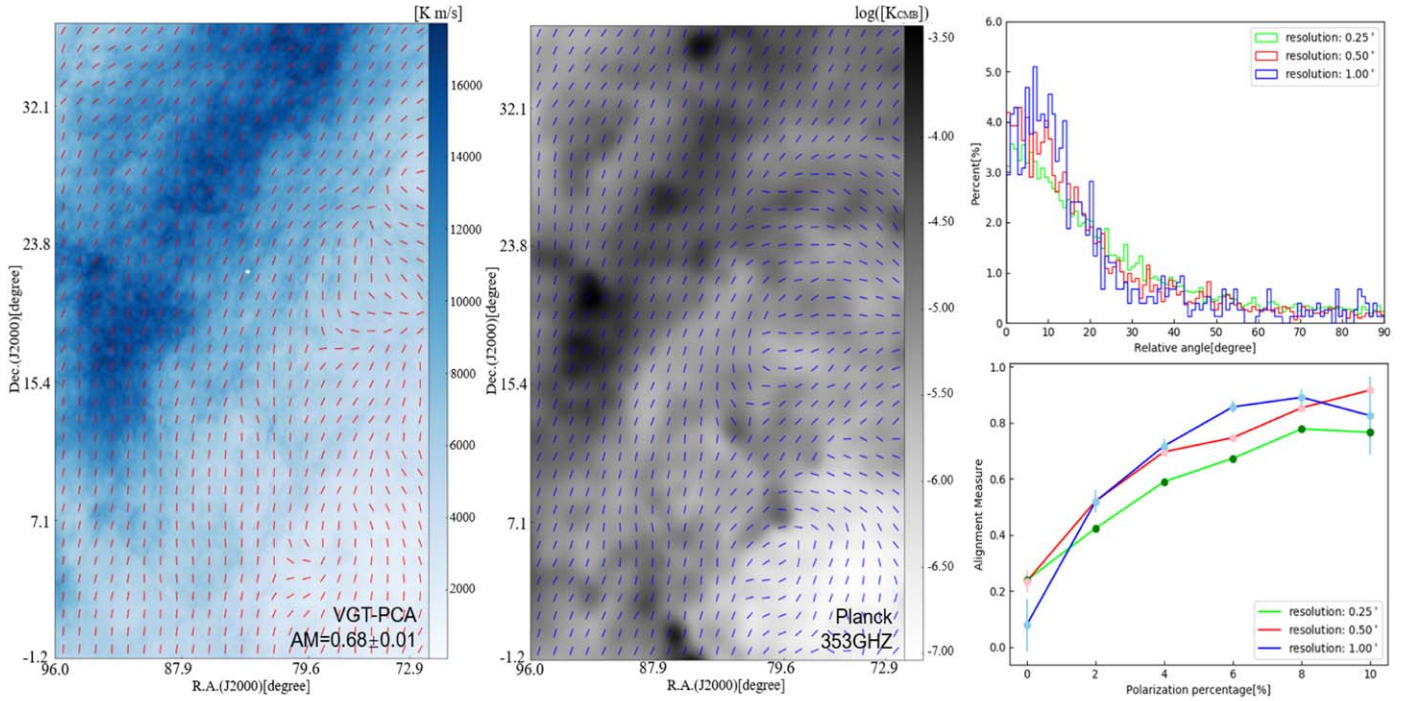

(a) A4

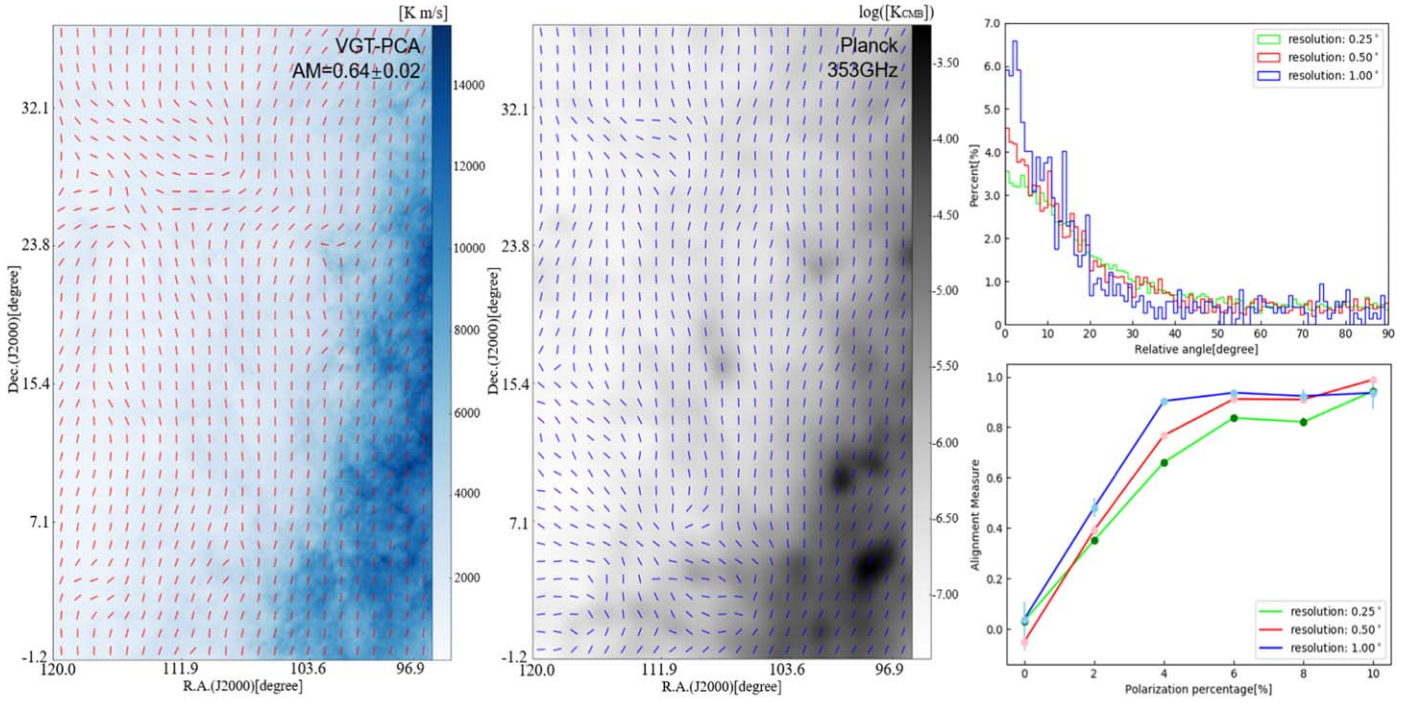

(b) A5

Figure 12. The morphology of the POS magnetic fields on the sky patch with (a): R.A. from 72.°0 to 96.°0 and decl. from −1.°2 to 37.°1, and (b): R.A. from 96.°0 to 120.°0 and decl. from −1.°2 to 37.°1. Left: the magnetic field predicted from VGT–PCA (red segments) with resolution ≃1°. Middle: the magnetic fields inferred from *Planck* polarization (blue segments). Right top: the histogram of the relative orientation between the magnetic field predicted by VGT–PCA and the one inferred from *Planck* polarization. Right bottom: the variation of the AM with respect to the polarization percentage.

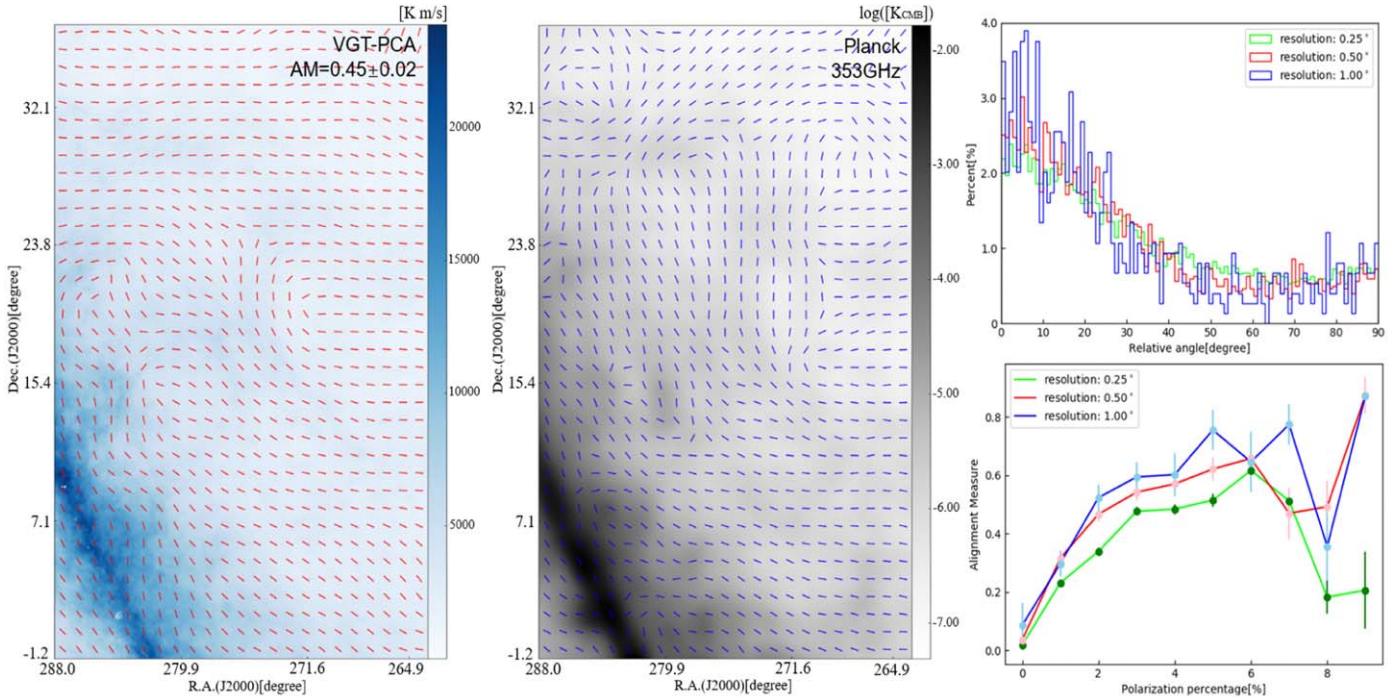

(a) C2

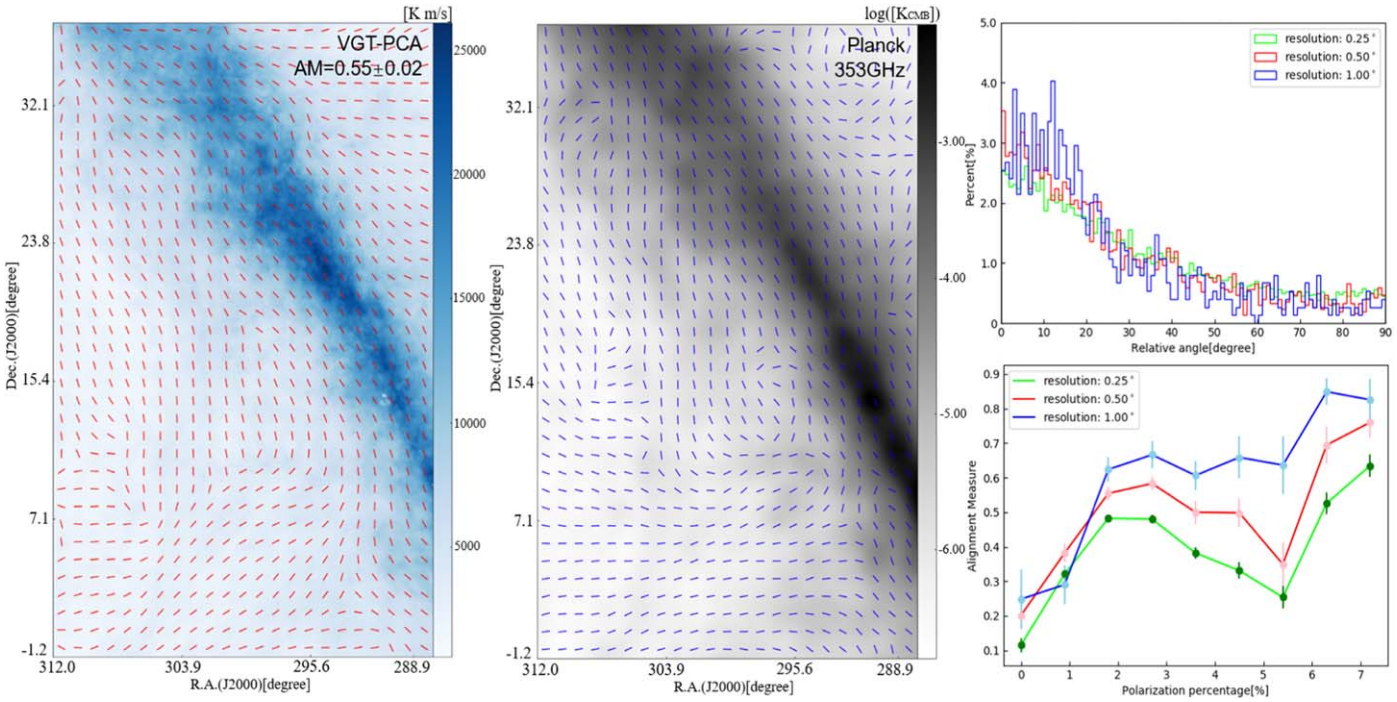

(b) C3

Figure 13. The morphology of the POS magnetic fields on the sky patch with (a): R.A. from 264.°0 to 288.°0 and decl. from −1.°2 to 37.°1, and (b): R.A. from 288.°0 to 312.°0 and decl. from −1.°2 to 37.°1. Left: the magnetic field predicted from VGT–PCA (red segments) with resolution ≃1°. Middle: the magnetic fields inferred from *Planck* polarization (blue segments). Right top: the histogram of the relative orientation between the magnetic field predicted by VGT–PCA and the one inferred from *Planck* polarization. Right bottom: the variation of the AM with respect to the polarization percentage.

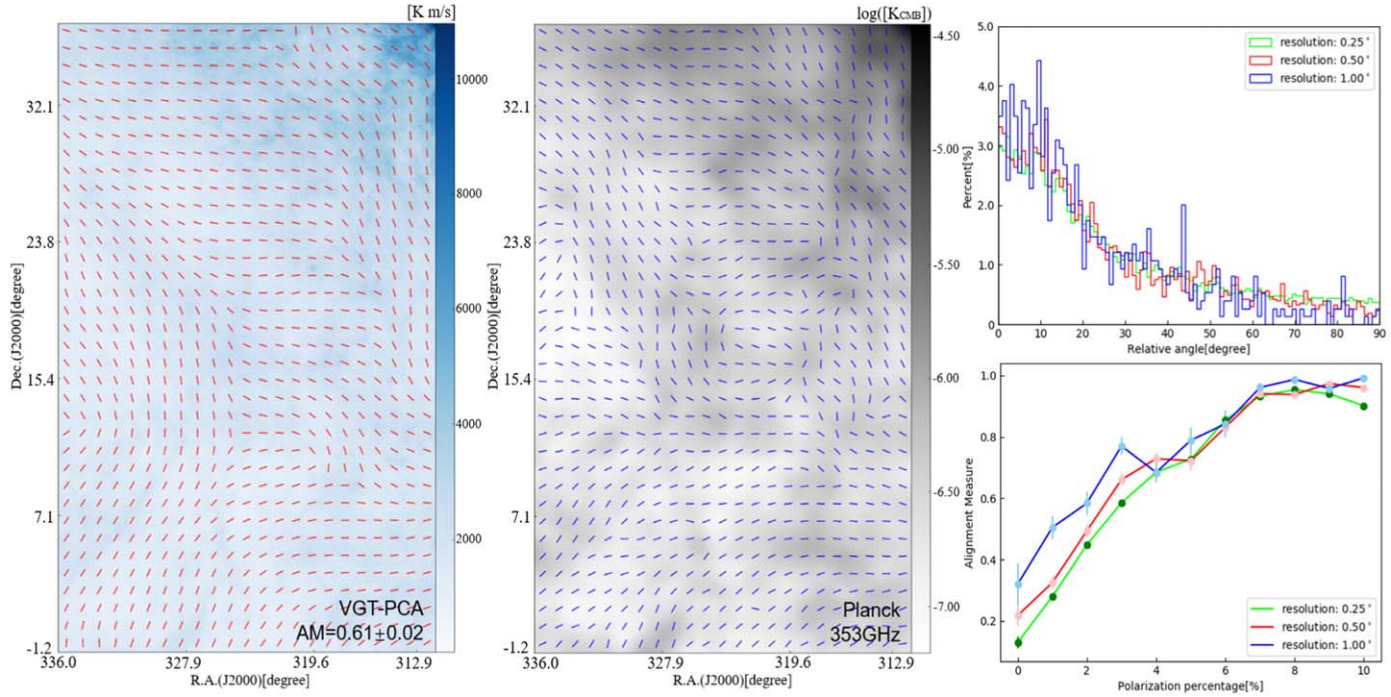

(a) C4

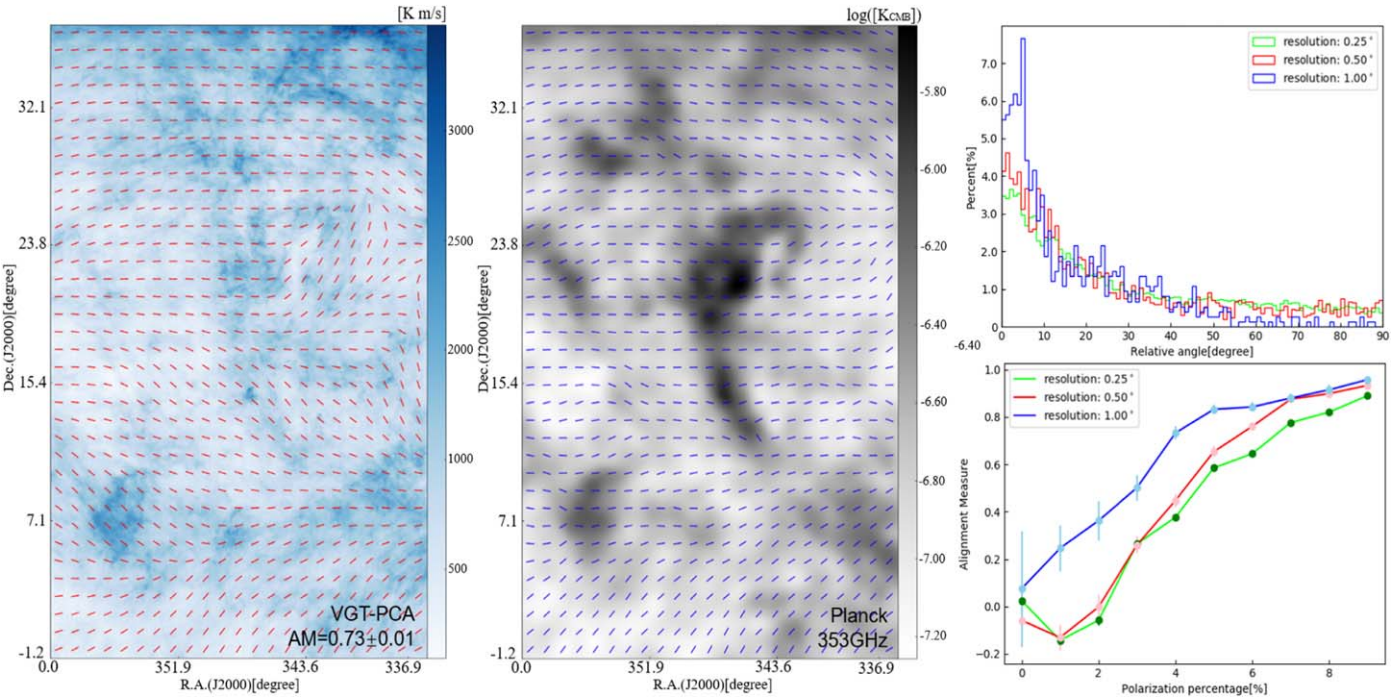

(b) C5

Figure 14. The morphology of the POS magnetic fields on the sky patch with (a): R.A. from 312.°0 to 336.°0 and decl. from −1.°2 to 37.°1, and (b): R.A. from 336.°0 to 360.°0 and decl. from −1.°2 to 37.°1. Left: the magnetic field predicted from VGT–PCA (red segments) with resolution ≃1°. Middle: the magnetic fields inferred from *Planck* polarization (blue segments). Right top: the histogram of the relative orientation between the magnetic field predicted by VGT–PCA and the one inferred from *Planck* polarization. Right bottom: the variation of the AM with respect to the polarization percentage.

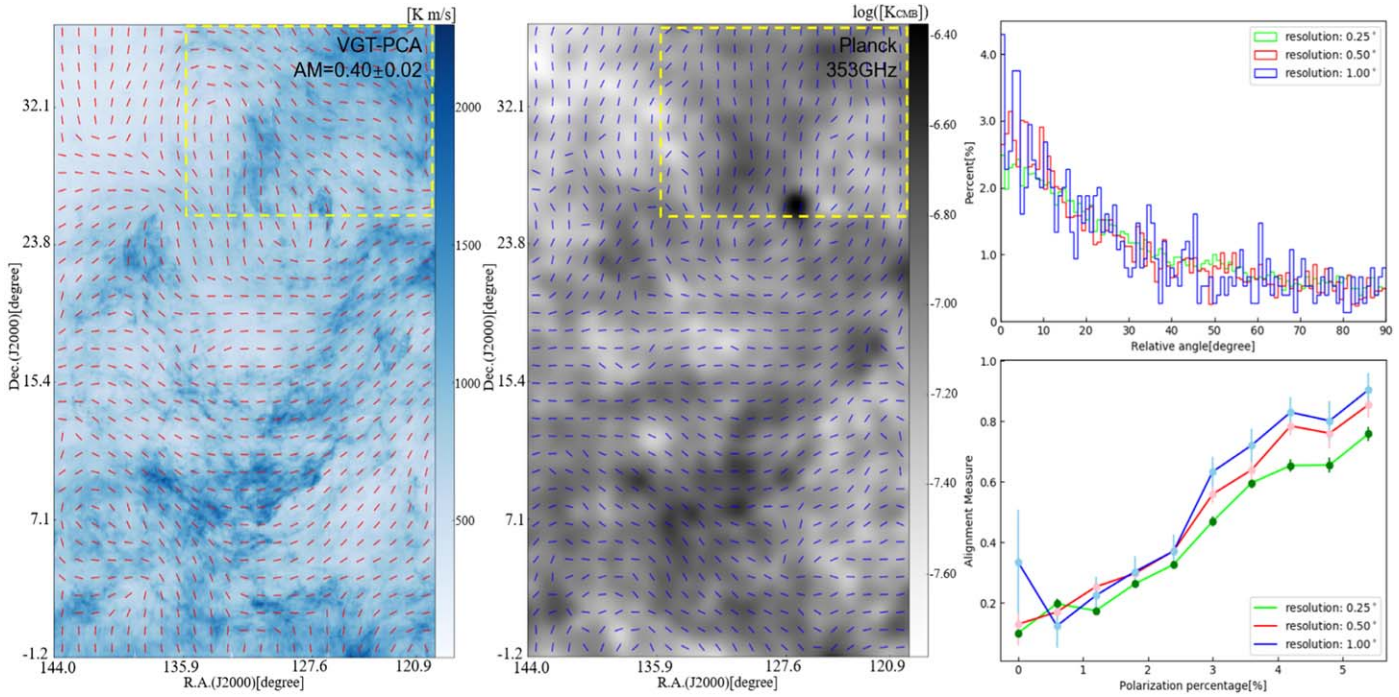

(a) B1

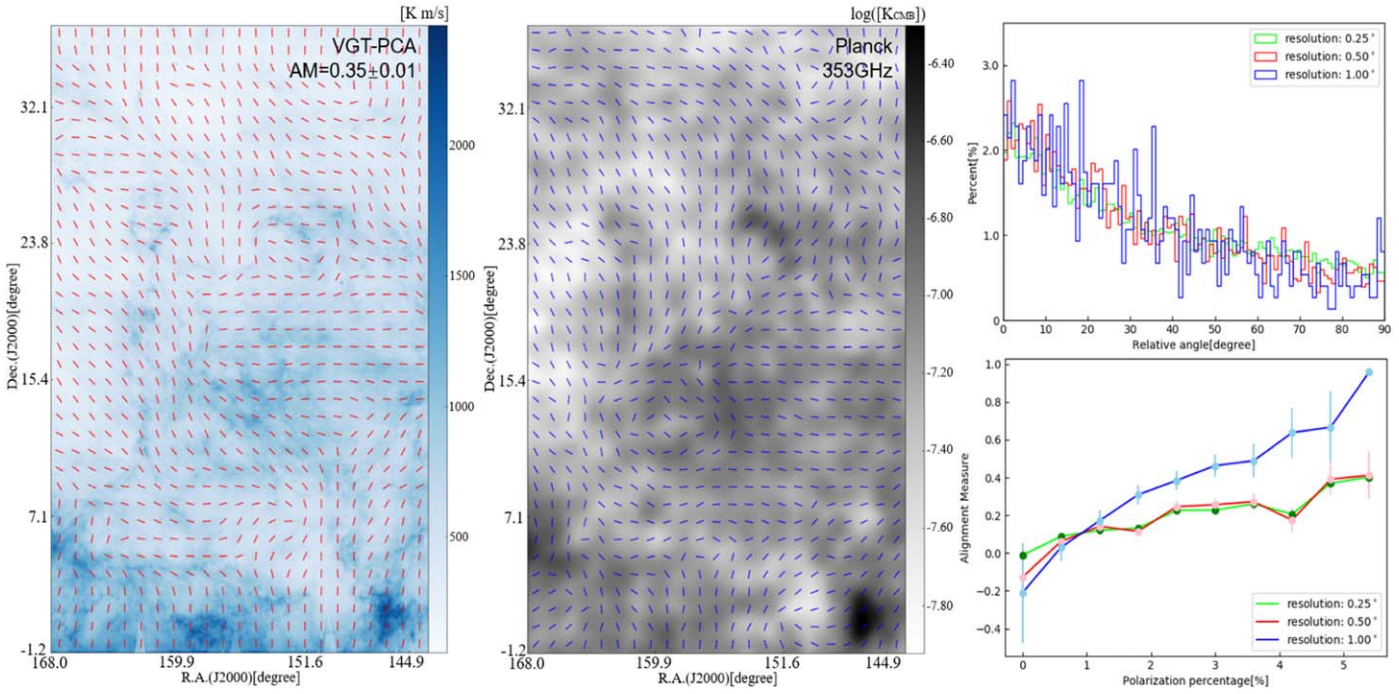

(b) B2

Figure 15. The morphology of the POS magnetic fields on the sky patch with (a): R.A. from 120.°0 to 144.°0 and decl. from −1.°2 to 37.°1, and (b): R.A. from 144.°0 to 360.°0 and decl. from −1.°2 to 37.°1. Left: the magnetic field predicted from VGT–PCA (red segments) with resolution ≃1°. Middle: the magnetic fields inferred from *Planck* polarization (blue segments). Right top: the histogram of the relative orientation between the magnetic field predicted by VGT–PCA and the one inferred from *Planck* polarization. Right bottom: the variation of the AM with respect to the polarization percentage.

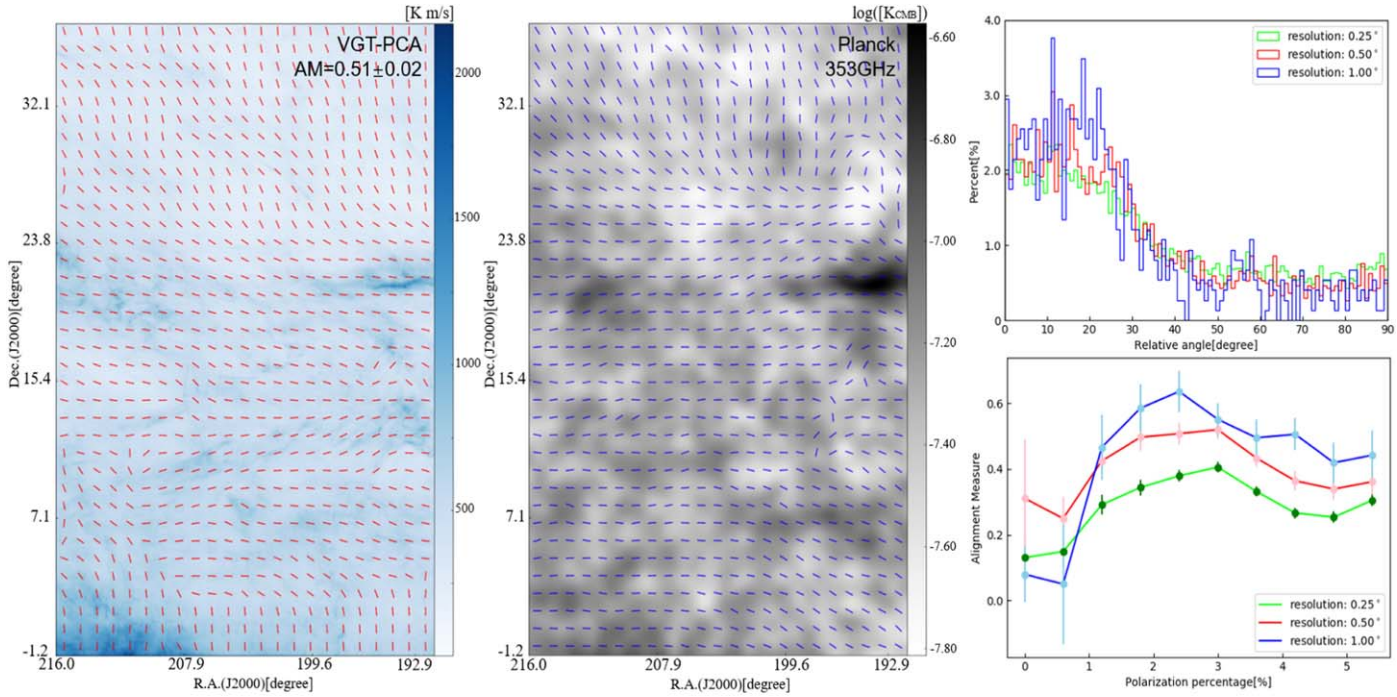

(a) B4

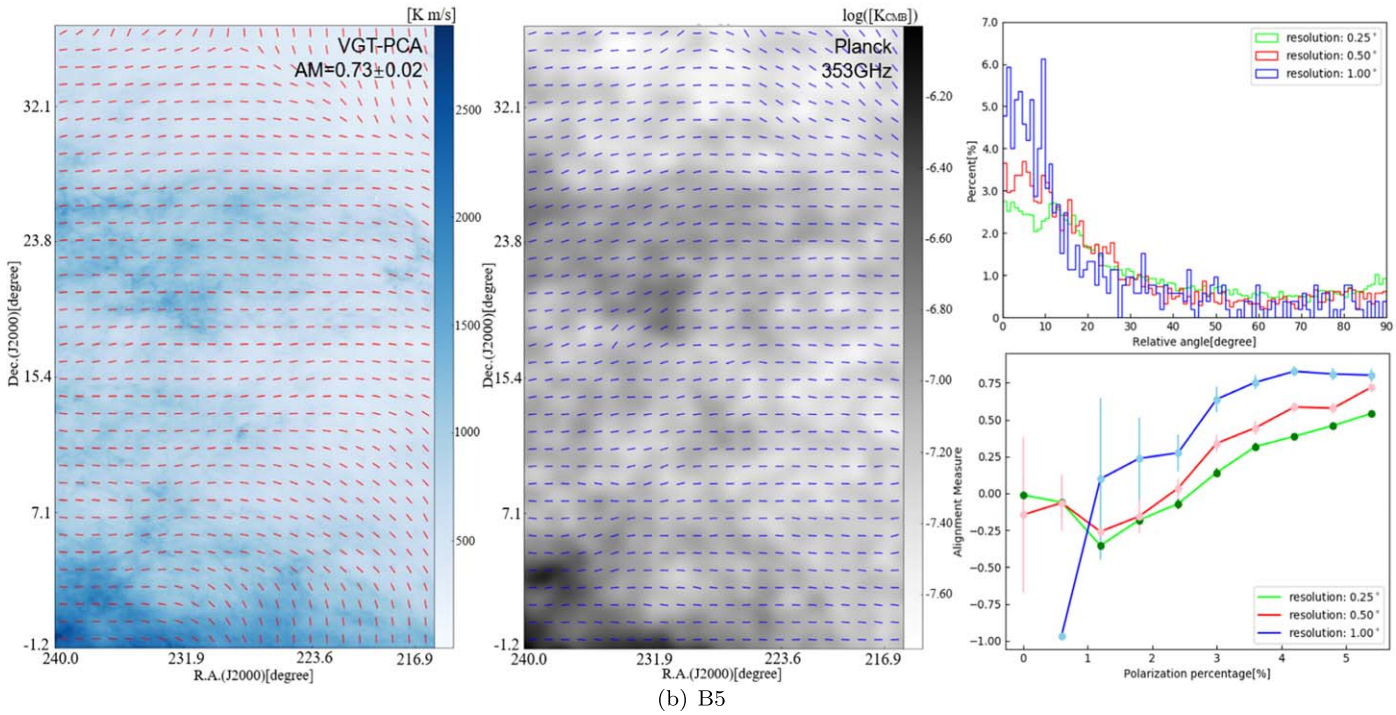

(b) B5

Figure 16. The morphology of the POS magnetic fields on the sky patch with (a): R.A. from 192.°0 to 216.°0 and decl. from −1.°2 to 37.°1, and (b): R.A. from 216.°0 to 240.°0 and decl. from −1.°2 to 37.°1. Left: the magnetic field predicted from VGT–PCA (red segments) with resolution ≃1°. Middle: the magnetic fields inferred from *Planck* polarization (blue segments). Right top: the histogram of the relative orientation between the magnetic field predicted by VGT–PCA and the one inferred from *Planck* polarization. Right bottom: the variation of the AM with respect to the polarization percentage.

its maximum deviation from 0° at high-latitude regions, i.e., B2, B3, B4. Also, μ shows a discrepancy when getting close to the Galactic plane, i.e., A4, C2, C3. We propose the existence of molecular clouds near the Galactic plane is one possible reason, because molecular clouds contribute to the dust polarization but not the H I.

Appendix B
Simulation Results

We numerically test the ability of the VGT–PCA technique in predicting dust polarization. The numerical 3D MHD simulations are generated by the ZEUS-MP/3D code (Hayes et al. 2006), which uses a single-fluid, operator-split, staggered-grid

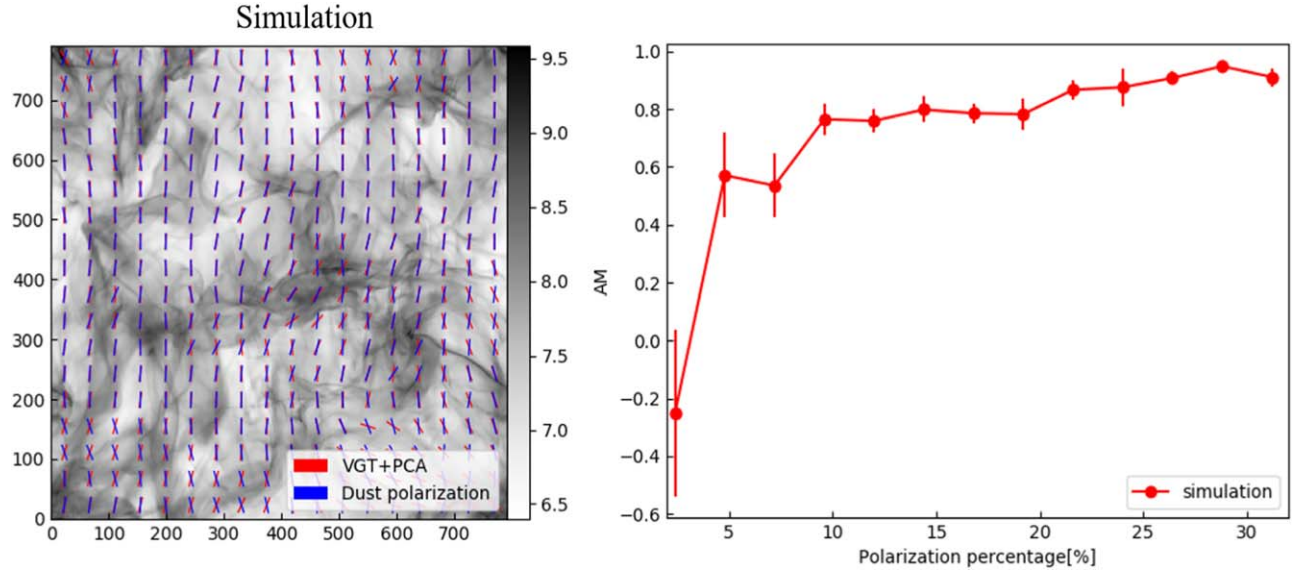

Figure 17. The numerical testing results of predicting the dust polarization through the VGT–PCA technique. Left: the magnetic fields obtained from VGT–PCA (red segments) and dust polarization (blue segments), with overall AM = 0.78 ± 0.03. The MHD simulation imposes $M_S = 6.14$ and Alfvén Mach number $M_A = 0.82$. Right: the variation of the AM with respect to the polarization percentage.

MHD Eulerian assumption. To emulate a part of the interstellar cloud, the periodic boundary conditions and solenoidal turbulence injections are applied in our simulations. We simulate the MHD turbulence using the barotropic equation of state, i.e., these clouds are isothermal with temperature $T = 10.0$ K, sound speed $c_s = 187\,\mathrm{m\,s^{-1}}$, cloud size $L = 10$ pc, and initial density $\rho_0 \sim 884.23\,\mathrm{cm^{-3}}$. The sonic Mach number M_S is 6.14 and the Alfvén Mach number M_A is 0.82 in our simulation.

We follow the recipe used in Section 3 to calculate the magnetic field morphology through either VGT–PCA or dust polarization. As shown in Figure 17, the numerical results also confirm the robust ability of VGT–PCA in predicting dust polarization, with overall AM = 0.78 ± 0.03. We also plot the correlation between polarization percentage p defined in Equation (2) and the AM in the corresponding regions. In Figure 17, we find that the correlation coincides with the observational results, i.e., the AM is positively proportional to the polarization percentage when $p < 10\%$. The AM gradually gets saturated when $p > 10\%$. It therefore numerically demonstrated our conclusion that insufficient polarization percentage or low dust grain alignment efficiency would cause the discrepancy between the magnetic fields obtained from gradients and dust polarization.

ORCID iDs

Yue Hu https://orcid.org/0000-0002-8455-0805
Ka Ho Yuen https://orcid.org/0000-0003-1683-9153

References

Ahrens, J., Geveci, B., & Law, C. 2005, Paraview: An End-user Tool for Large Data Visualization, Vol. 717 (Oxford: Elsevier)
Berdyugin, A., Piirola, V., & Teerikorpi, P. 2014, A&A, 561, A24
Bezanson, J., Karpinski, S., Shah, V. B., et al. 2012, arXiv:1209.5145
BICEP2 Collaboration, Ade, P. A. R., Aikin, R. W., et al. 2014, PhRvL, 112, 241101
Brunt, C. M., & Heyer, M. H. 2002a, ApJ, 566, 276
Brunt, C. M., & Heyer, M. H. 2002b, ApJ, 566, 289
Cho, J., & Lazarian, A. 2002, PhRvL, 88, 245001
Cho, J., & Lazarian, A. 2003, MNRAS, 345, 325
Cho, J., & Vishniac, E. T. 2000, ApJ, 539, 273
Clark, S. E., & Hensley, B. S. 2019, ApJ, 887, 136
Clark, S. E., Hill, J. C., Peek, J. E. G., et al. 2015, PhRvL, 115, 241302
Clark, S. E., Peek, J. E. G., & Putman, M. E. 2014, ApJ, 789, 82
Ferreira, R. J. Z., Jain, R. K., & Sloth, M. S. 2014, JCAP, 6, 053
Goldreich, P., & Kylafis, N. D. 1982, ApJ, 253, 606
Goldreich, P., & Sridhar, S. 1995, ApJ, 438, 763
González-Casanova, D. F., & Lazarian, A. 2017, ApJ, 835, 41
González-Casanova, D. F., & Lazarian, A. 2019, ApJ, 874, 25
González-Casanova, D. F., Lazarian, A., & Burkhart, B. 2019, MNRAS, 483, 1287
Górski, K. M., Hivon, E., Banday, A. J., et al. 2005, ApJ, 622, 759
Hanany, S., Alvarez, M., Artis, E., et al. 2019, BAAS, 51, 194
Hayes, J. C., Norman, M. L., Fiedler, R. A., et al. 2006, ApJS, 165, 188
Heyer, M., Gong, H., Ostriker, E., & Brunt, C. 2008, ApJ, 680, 420
Hotelling, H. 1933, Journal of Educational Psychology, 24, 417
Hsieh, C.-H., Hu, Y., Lai, S.-P., et al. 2019, ApJ, 873, 16
Hu, Y., Yuen, K. H., & Lazarian, A. 2018, MNRAS, 480, 1333
Hu, Y., Yuen, K. H., Lazarian, A., et al. 2019a, ApJ, 884, 137
Hu, Y., Yuen, K. H., & Lazarian, A. 2019b, ApJ, 886, 17
Hu, Y., Yuen, K. H., Lazarian, V., et al. 2019c, NatAs, 3, 776
Jones, T. J. 1989, ApJ, 346, 728
Kalberla, P. M. W., & Haud, U. 2018, A&A, 619, A58
Kamionkowski, M., & Kovetz, E. D. 2016, ARA&A, 54, 227
Kandel, D., Lazarian, A., & Pogosyan, D. 2017, MNRAS, 464, 3617
Kovetz, E. D., & Kamionkowski, M. 2015, PhRvD, 91, 81303
Lazarian, A. 2003, JQSRT, 79, 881
Lazarian, A., & Hoang, T. 2007, ApJL, 669, L77
Lazarian, A., & Hoang, T. 2019, ApJ, 883, 122
Lazarian, A., & Pogosyan, D. 2000, ApJ, 537, 720
Lazarian, A., & Pogosyan, D. 2004, ApJ, 616, 943
Lazarian, A., & Vishniac, E. T. 1999, ApJ, 517, 700
Lazarian, A., & Yuen, K. H. 2018a, ApJ, 853, 96
Lazarian, A., & Yuen, K. H. 2018b, ApJ, 865, 59
Lazarian, A., Yuen, K. H., Ho, K. W., et al. 2018a, ApJ, 865, 46
Lazarian, A., Yuen, K. H., Lee, H., et al. 2018b, ApJ, 855, 72
Lee, A., Ade, P. A. R., Akiba, Y., et al. 2019, BAAS, 51, 286
Lewis, A. 2003, PhRvD, 68, 83509
Lu, Z., Lazarian, A., & Pogosyan, D. 2019, MNRAS, submitted (arXiv:1910.02226)
Manzotti, A., Story, K. T., Wu, W. L. K., et al. 2017, ApJ, 846, 45
Maron, J., & Goldreich, P. 2001, ApJ, 554, 1175
Peek, J. E. G., Babler, B. L., Zheng, Y., et al. 2018, ApJS, 234, 2
Planck Collaboration, Abergel, A., Ade, P. A. R., et al. 2014a, A&A, 571, A11
Planck Collaboration, Abergel, A., Ade, P. A. R., et al. 2014b, A&A, 566, A55
Planck Collaboration, Adam, R., Ade, P. A. R., et al. 2016a, A&A, 594, A10

Planck Collaboration, Adam, R., Ade, P. A. R., et al. 2016b, A&A, 594, A9
Planck Collaboration, Adam, R., Ade, P. A. R., et al. 2016c, A&A, 586, A133
Planck Collaboration, Ade, P. A. R., Aghanim, N., et al. 2015a, A&A, 576, A105
Planck Collaboration, Ade, P. A. R., Aghanim, N., et al. 2015b, A&A, 576, A104
Planck Collaboration, Ade, P. A. R., Aghanim, N., et al. 2016d, A&A, 586, A141
Planck Collaboration, Aghanim, N., Akrami, Y., et al. 2018a, A&A, in press (arXiv:1807.06207)
Planck Collaboration, Aghanim, N., Akrami, Y., et al. 2018b, A&A, in press (arXiv:1807.06212)
Planck Collaboration, Aghanim, N., Arnaud, M., et al. 2016e, A&A, 594, A11
Planck Collaboration, Akrami, Y., Ashdown, M., et al. 2018c, A&A, in press (arXiv:1801.04945)
Remazeilles, M., Banday, A. J., Baccigalupi, C., et al. 2018, JCAP, 2018, 023
Voshchinnikov, N. V., Il'in, V. B., & Das, H. K. 2016, MNRAS, 462, 2343
Yuen, K. H., Chen, J., Hu, Y., et al. 2018, ApJ, 865, 54
Yuen, K. H., Hu, Y., Lazarian, A., et al. 2019, arXiv:1904.03173
Yuen, K. H., & Lazarian, A. 2017a, ApJL, 837, L24
Yuen, K. H., & Lazarian, A. 2017b, arXiv:1703.03026
Zhang, J.-F., Lazarian, A., Ho, K. W., et al. 2019, MNRAS, 486, 4813